

THESIS FOR THE DEGREE OF LICENTIATE OF ENGINEERING

# Materials and Coatings for Superheater Tubes in Biomass- and Waste-fired Boilers

Insights into long-term high-temperature corrosion behaviour

Vicent Ssentenza



Department of Chemistry and Chemical Engineering

CHALMERS UNIVERSITY OF TECHNOLOGY

Gothenburg, Sweden 2023

Materials and Coatings for Superheater Tubes in Biomass- and Waste-fired Boilers  
Insights into long-term high-temperature corrosion behaviour

Vicent Ssentenza

© Vicent Ssentenza, 2023.

Thesis for the degree of Licentiate of Engineering  
Nr: 2023:05  
Department of Chemistry and Chemical Engineering  
Chalmers University of Technology  
SE-412 96 Gothenburg  
Sweden  
Telephone + 46 (0)31-772 1000

Cover: SEM-BSE cross-section images of martensitic stainless steel (to the left) and an austenitic stainless steel (to the right) showing oxide microstructure after exposure to 5% O<sub>2</sub> + 20% H<sub>2</sub>O + N<sub>2</sub> (Bal) + KCl(s)/KCl(g) for 8,000 hours at 600°C.

Printed by Chalmers Reproservice  
Gothenburg, Sweden 2023

## Abstract

Combustion of biomass and waste fuels has strong potential as an alternative renewable energy source for meeting the increasing global energy demand, while reducing the net release of CO<sub>2</sub> into the atmosphere. The combustion of biomass and waste releases flue gases that contain high amount of alkali salts and water vapour, which drive the corrosion of metallic boiler components. Corrosion issues can lead to reduced material life-time, costly boiler system failures, and eventually reduced electricity efficiency. The focus of corrosion research in these environments has primarily been on the initiation of corrosion and short-term exposures. However, to combat corrosion, it is important to gain an in-depth understanding of the corrosion behaviour of the material during long-term exposure.

For this work, a novel experimental set-up that mimics the corrosive nature of the boiler environment was developed, to investigate the long-term corrosion behaviours of materials and coatings. Several relevant chromia- and alumina-forming alloys were exposed as bulk materials and as overlay weld coatings in a KCl(s)/KCl(g)-rich environment at 600°C. The corrosion behaviours were investigated using advanced ion and electron microscopy, together with thermodynamic equilibrium calculations and kinetic simulations.

The results show that all alloys experience breakaway oxidation and transition into a secondary corrosion regime, i.e., forming double-layered oxide scales (outward- and inward-growing scales). Within the secondary corrosion regime, alloys may form either fast-growing and less-protective scales (poor secondary protection) or slow-growing and more-protective scales (good secondary protection), depending on the oxide microstructure formed after the breakaway process. The oxide microstructure is influenced by the content of alloying elements, as well as by the microstructure of the alloy. Bulk materials exhibit better corrosion resistance than the overlay weld coatings of similar composition, due to faster formation of the protective secondary scale. The results also indicate that the high-alloy steels experience phase transformation in the inward-growing scales from a less-protective spinel oxide to a more-protective corundum-type oxide, which leads to better corrosion resistance during long exposures.

**Keywords:** High-Temperature Corrosion, Boiler, Biomass, Waste, Breakaway Oxidation, Secondary Protection, Phase transformation

# List of publications

The thesis is based on the following papers:

## Paper I

V. Ssentenza, J. Eklund, I. Hanif, J. Liske, and T. Jonsson, “High temperature corrosion resistance of FeCr(Ni, Al) alloys as bulk/overlay weld coatings in the presence of KCl at 600°C,” *Corros Sci*, vol. 213, p. 110896, Apr. 2023, **Doi: 10.1016/J.CORSCI.2022.110896.**

## Paper II

I. Hanif, V. Ssentenza, J. Eklund, J. Nockert, T. Jonsson, “High-Temperature Corrosion of Weld Overlay Coating/Bulk FeCrAl Exposed in O<sub>2</sub> + H<sub>2</sub>O + KCl(s) at 600°C – A Microstructural Investigation,” **Submitted to Material Research and Technology (2023)**

## Paper III

V. Ssentenza, J. Eklund, S. Bigdeli, I. Hanif and T. Jonsson, “Long-term corrosion behavior of FeCr(Al, Ni) alloys in O<sub>2</sub> + H<sub>2</sub>O with KCl(s) at 600°C: Microstructural evolution after breakaway oxidation,” **Submitted to Corrosion Science (2023)**

## Statement of the author’s contribution

For all the included papers, I performed the experimental work. I was the principal author of papers I and III. PhD Sedigheh Bigdeli was responsible for the computational thermodynamic and kinetic calculations in paper III. Besides the experimental work, I was also responsible for some data curation in paper II.

## **Related work and technical reports not included in this thesis**

J. Eklund, A. Persdotter, V. Ssentenza, T. Jonsson, “The long-term corrosion behaviour of FeCrAl(Si) alloys after breakaway oxidation at 600 °C, ” Corros Sci. 217 (2023) 111155.  
**Doi: 10.1016/j.corsci.2023.111155.**

# Acknowledgments

Firstly, I would like to express my gratitude to my supervisors Dr. Torbjörn Jonsson, Assoc. Prof. Jesper Liske and Prof. Jan-Erik Svensson for all the support, the time and the discussions we had during this work. You have been inspirational and kept me on track all the time.

A big thank you to Dr. Johan Eklund for sharing with me your practical and theoretical knowledge within high-temperature corrosion, and the fun times we had from the start of my PhD.

I also acknowledge The European Commission for the financial support, Alleima AB, Kanthal AB and Vallourec SA for supplying materials and coatings for this work, High-Temperature Corrosion Centre (HTC), the CMAL group for the technical support regarding microscopy.

I am very thankful to all my colleagues for the encouragement, scientific and non-scientific discussions. Fika times have always been fun! Thank you, Dr. Dolores Paz Olausson and Sandra Nayeri, for your help with practical and administrative stuff.

Finally, a special thank you to my family for your understanding during this work. It has been tough, but you kept me on my feet and are a big part of this achievement. My wife, Edlira Ssentenza, I am forever grateful 😊!

*Vicent Ssentenza, Gothenburg (2023)*

## Table of Contents

|   |    |
|---|----|
| 1. Introduction .....   | 1  |
| 2. Combined heat and power (CHP) plants.....                        | 3  |
| 2.1 Biofuels and waste.....   | 3  |
| 2.2 Biomass- and waste-fired boilers .....                          | 5  |
| 3. Materials .....  | 7  |
| 3.1 Alloy classification based on content of alloying elements..... | 7  |
| 3.2 Alloy classification based on scale formation. ....             | 7  |
| 3.2.1 Chromia-forming alloys.....                                   | 7  |
| 3.2.2 Alumina-forming alloys .....                                  | 8  |
| 3.3 Alloys used in this study.....                                  | 8  |
| 3.3.1. Bulk materials.....  | 9  |
| 3.3.2. Coatings.....  | 10 |
| 4. High-temperature corrosion .....                                 | 13 |
| 4.1 Oxidation of metals.....  | 13 |
| 4.1.1 Thermodynamics.....   | 13 |
| 4.1.2 Kinetics .....  | 14 |
| 4.2 Corrosion regimes.....  | 16 |
| 4.1.1 Primary protection .....                                      | 16 |
| 4.1.2 Breakaway oxidation.....                                      | 16 |
| 4.1.3 Secondary protection.....                                     | 17 |
| 4.3 Corrosion mechanisms .....                                      | 18 |
| 4.2.1 Chlorine-induced corrosion – “chlorine cycle” .....           | 18 |
| 4.2.4 Chlorine-induced corrosion – “electrochemical approach” ..... | 19 |
| 4.2.2 Chromate formation .....                                      | 19 |
| 4.2.3 Chromic acid formation .....                                  | 19 |
| 5. Experimental section.....  | 21 |
| 5.1 Set-up development .....  | 21 |
| 5.1.1 KCl evaporation.....  | 21 |
| 5.1.2 Robustness study .....  | 22 |
| 5.2 Long-term exposures .....                                       | 22 |
| 5.2.1 Materials .....   | 22 |
| 5.2.2. Sample preparation and exposures .....                       | 23 |
| 6. Analytical techniques .....                                      | 25 |
| 6.1 Cross-section preparation - broad ion beam (BIB) milling .....  | 25 |

|  |    |
|--|----|
| 6.2 Light Optical microscopy (LOM).....                                    | 25 |
| 6.3 Scanning electron microscopy (SEM) .....                               | 26 |
| 6.4 Electron backscatter diffraction (EBSD).....                           | 28 |
| 6.5 Transmission electron microscopy (TEM).....                            | 29 |
| 6.6 X-ray diffraction (XRD) .....  | 29 |
| 6.7 Average grain size measurement .....                                   | 29 |
| 6.8 Computational modelling and simulation .....                           | 30 |
| 7. Results and Discussion .....  | 31 |
| 7.1 State-of-the-art exposures for long-term corrosion investigations..... | 31 |
| 7.1.1 Conditions to mimic the boiler environment.....                      | 31 |
| 7.1.2 Robustness of the set-up .....                                       | 32 |
| 7.2 Long-term corrosion behaviours of bulk materials and coatings .....    | 33 |
| 7.2.1 Corrosion resistance .....   | 33 |
| 7.2.2 Why bulk materials perform better than overlay weld coatings.....    | 37 |
| 7.2.3 Microstructural evolution after breakaway oxidation.....             | 42 |
| 8. Conclusion .....  | 51 |
| 9. Future work.....  | 53 |
| 10. Reference .....  | 55 |

# 1. Introduction

The increasing global demand for energy is a driving force for innovation and improvements in relation to the infrastructure of the energy sector. As the world population increases and new cities emerge, the demand for energy is increasing. According to statistics released by the International Energy Agency (IEA) [1], the total global level of energy consumed in Year 2019 was 418 EJ (see Figure 1.1), and the projection is that double the current energy level will be needed by Year 2040. Currently, fossil fuels such as oil and coal are the main sources for electricity generation. However, the use of fossil fuels has led to increased emissions of greenhouse gases, such as CO<sub>2</sub> and N<sub>2</sub>O, which are linked to global warming [2–4]. To combat climate change, there is an urgent need to find alternative energy sources that offer energy security and have a reduced impact on climate change.

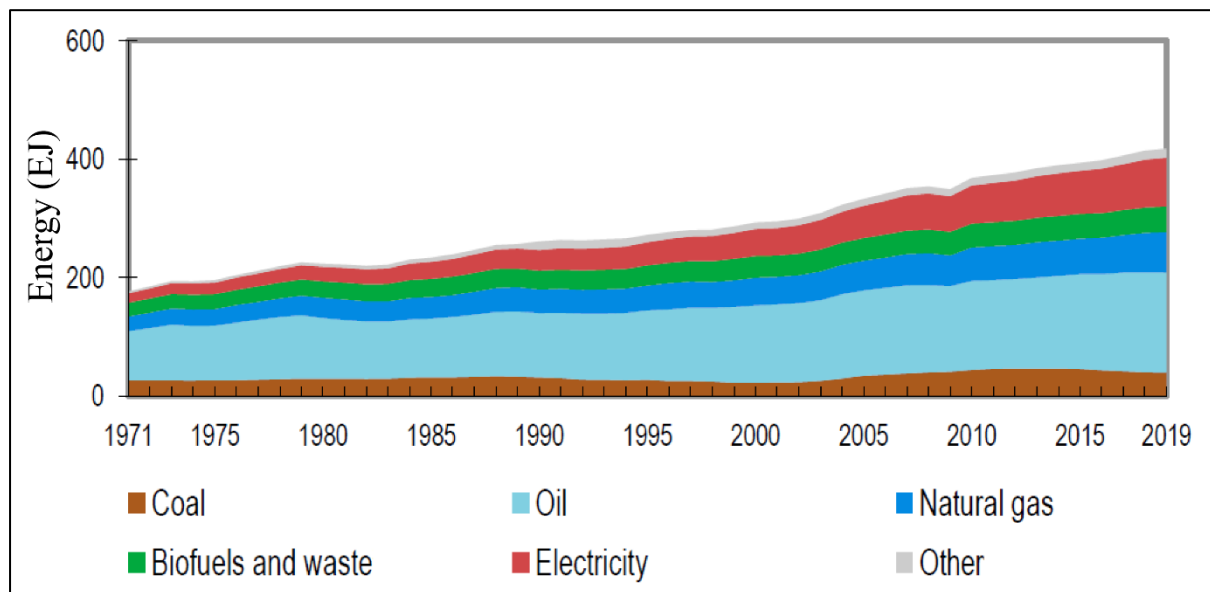


Figure 1.1: World total energy supply by source in EJ (1EJ = 277.8 TWh) [1]

One solution is to use renewable energy sources, such as wind energy, solar energy, bioenergy, geothermal energy, and hydropower. Currently, renewable energy sources constitute only about 12% of the total global energy supply, with biofuels making the largest contribution (10.2%). Biofuels derived from biomass and waste have great potential as alternative energy sources and have been incorporated into many energy policies around the world to meet high energy demands. Biomass and waste are used for combined heat and power (CHP) production on both small and large scales. Over the last decades, advances have been made in the CHP technology that have resulted in improved boiler performance. For example, the advanced secondary air supply [5] and the integrated biomass multi-stage gasification system [6] have enhanced the conversion of fuel particles. However, the efficiency of electricity generation from the combustion of biomass and waste is relatively low, compared to generation from fossil fuels. One challenge associated with the combustion of biofuels is the accelerated corrosion of metallic components of the boilers (e.g., the super-heater tubes). It is well-established in the literature that the accelerated corrosion experienced in the boiler environment is mainly due to corrosive species, such as KCl, HCl, and H<sub>2</sub>O, which are formed during the combustion of biofuels [7–23]. These species may break down the protective scales of the metal (i.e., primary protection) in the breakaway process, leading to the formation of fast-growing, multi-layered

scales that are less-protective (i.e., secondary protection). Corrosion issues in the boiler lead to rapid material degradation, tube failures, costly unplanned plant shutdowns, and reduced efficiency of electricity generation.

Several solutions have been proposed to mitigate corrosion in biomass-fired and waste-fired boilers. One strategy is to reduce the steam temperature of the boiler, which leads to a lower material temperature and reduced corrosion. Another approach is to use additives, e.g., ammonium sulphate, which mitigates KCl-induced corrosion [24]. The use of materials and coatings such as stainless steels ( $>10.5$  wt% Cr), which may offer better corrosion resistance than the low-alloyed steels, has been applied in many boilers. However, as new fuel feedstocks containing high levels of corrosive species emerge, it becomes necessary to understand the corrosion behaviours of materials and coatings designed for applications in these environments. Specifically, knowledge of the underlying corrosion mechanism and of the formation of good secondary protection during long-term operation may suggest criteria for the selection of optimally performing materials. Currently, there are few well-controlled, long-term laboratory investigations and studies on the detailed microstructural evolution of the oxide scales formed in environments relevant to boiler applications.

Therefore, the aim of this thesis is to contribute with knowledge regarding the long-term corrosion behaviours of materials and coatings for applications in biomass-fired and waste-fired boilers. This was achieved by developing an experimental set-up in which corrosive species (KCl) can be present on the sample surface during long exposures. The corrosion study was carried out by exposing FeCr(Ni, Al) alloys to an environment that consists of 5%  $O_2$  + 20%  $H_2O$  +  $N_2$  (Bal) + KCl(s)/KCl(g) at 600°C. Microstructural investigations were performed on cross-sections prepared using gentle sample preparation techniques such as broad ion beam (BIB) milling and focused ion beam (FIB) milling. The analyses were performed using scanning electron microscopy (SEM) in combination with energy-dispersive x-ray (EDX) spectroscopy, x-ray diffraction (XRD), electron back-scattered diffraction (EBSD) and transmission electron microscopy (TEM).

## 2. Combined heat and power (CHP) plants

Combined heat and power (CHP) plants deploy various technologies to produce electricity and useful heat from a variety of fuels. The electricity/heat produced by these plants is integrated into home, district, and industrial heating systems. Many of the CHP plants are based on the Rankine cycle process in which steam from the boiler is re-heated at a constant pressure to create high-pressure steam that is above the saturation point. The steam expands in the gas turbine, which produces useful work and runs the generator from which electricity is produced [25]. The produced heat is recovered using a waste heat recovery boiler and can be supplied to district heating. Fuel feedstocks such as coal, natural gas, biofuels, and waste can be combusted. During the combustion process, the operating parameters related to steam temperature and pressure must be carefully chosen to meet both the technical requirements and human safety rules.

According to a report issued by the European Commission's Directorate-General, the number of installed CHP units has been steadily increasing across the European Union (EU) since Year 2005, which has led to an increased electricity supply for the Member States [26]. Currently, most CHP plants operate under super-critical steam conditions in the Rankine cycle ( $>374^{\circ}\text{C}$ , 221 bar). A few coal-fired plants operate under ultra-super-critical (USC) steam conditions ( $>600^{\circ}\text{C}$ , 270 bar). However, no biomass-fired or waste-fired plants operate under USC conditions. The USC conditions yield higher efficiencies of electricity generation than the super-critical conditions. Depending on the type of fuel being combusted and the thermodynamic parameters of the process, different electricity efficiencies can be achieved. The average electricity generation efficiencies are in the ranges of. 27%–43% for coal; 31%–55% for natural gas; 23%–43% for oil; and 25%–37% biofuels [26,27]. **Error! Reference source not found.**1 provides an overview of the electricity generation efficiencies for the various fuels and combustion technologies and their associated operating parameters.

Although electrical efficiency from combustion of biofuels is low, these fuels present feasible options for meeting the increasing energy demands while reducing net greenhouse gas emissions. One challenge associated with the combustion of biofuels, which is one that affects the efficiency of electricity generation, is the severe corrosion of the metallic components of the boilers that occurs in the temperature range of  $450^{\circ}\text{--}580^{\circ}\text{C}$  (steam temperatures) [28]. This severe corrosive attack has been attributed to the presence of alkali salts that are created during the combustion of biofuels [8,10,19,20,22]. See Table 2.1 for the chemical compositions of the various fuels. Nonetheless, CHP based on the biofuel combustion technology is economically and environmentally viable. Therefore, it is worth exploring the potentials of biofuels as energy sources for the supply of small- and large-scale energy demands.

### 2.1 Biofuels and waste

Biofuels are fuels that are derived directly or indirectly from biomass, which originates from organic materials. The term ‘biomass’ covers a diversity of organic materials, which can be categorised into the following groups:

1. Solid biofuels (e.g., wood, agricultural products, waste etc.);
2. Liquid biofuels (e.g., biodiesel); and
3. Biogas (e.g., methane).

For CHP plants operating with biomass, solid biofuels are the most commonly used feedstocks, constituting about 70% of the total use of biomass for electricity generation [29]. Therefore, the focus of this study is on solid biofuels. Figure 2.1 provides a summary of the different sources of solid biofuels consumed in electricity generating plants within the EU. In recent decades, wood feedstocks have become the main source of energy, whereby they are combusted directly in the forms of wood chips, fellings, and bark or indirectly in the forms of saw-milling residues and by-products from the pulp and paper industry.

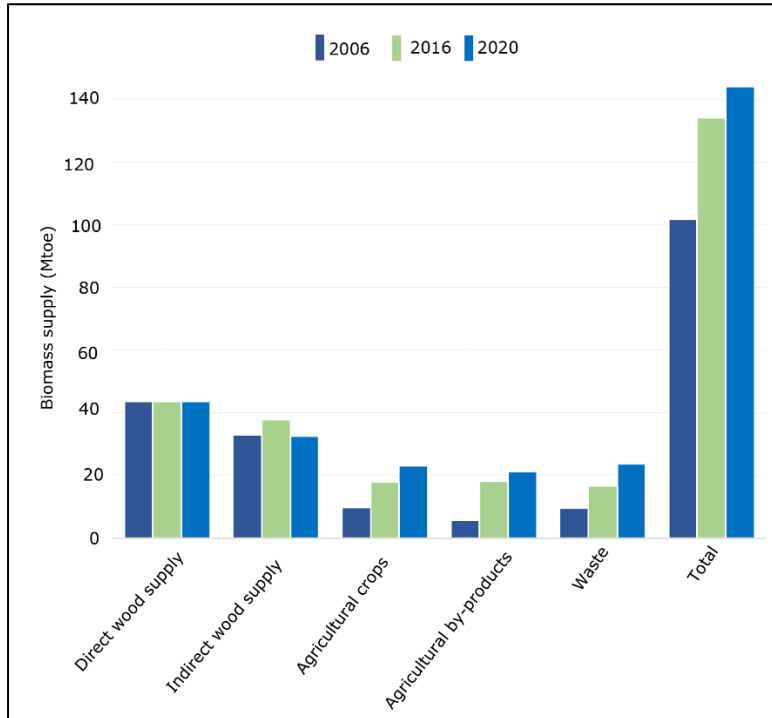


Figure 2.1: Sources of biomass for production of electricity within the EU. The data are based on progress reports from EU Member States and reported by the Joint Research Centre (JRC) [30].

Agricultural feedstocks, which include residues from agricultural harvesting and dedicated agricultural crops (e.g., straw and maize), show great potential as combustion materials. There are many advantages linked to using agricultural feedstocks, such as good availability and low cost of production. The potential of agricultural feedstocks for CHP plants is evident today, with 15 large CHP plants in the EU operating on straw and less than 8% of the theoretical potential of agricultural straw currently being exploited [31]. This indicates that straw will continue to have an important role in the energy sector.

Burnable bio-wastes, such as municipal solid waste (MSW), sludge, and waste from industrial processes may be used as feedstocks in CHP plants. These materials are collected and transported to collecting sites where they are sorted and distributed to the power plants. However, waste streams pose additional challenges for the combustion technology, as they exhibit diverse fuel characteristics and fractions (e.g., plastics, rubber, and electronics), which contain high levels of alkali salts, as well as heavy metals. Thus, the operating parameters for the boilers must be carefully chosen to ensure human safety and high conversion rates, while minimising corrosion and emissions of air pollutants.

Table 2.1: Compositions of various species in selected solid biofuels [32]

| Fuel type     | Species   |                        |          |         |               |                |
|---------------|-----------|------------------------|----------|---------|---------------|----------------|
|               | Ash (wt%) | H <sub>2</sub> O (wt%) | Cl (wt%) | S (wt%) | K (mg/kg) dry | Na (mg/kg) dry |
| Wood          | 0.6       | 15.9                   | 0.03     | <0.5    | 680           | 30             |
| Straw         | 8.6       | 10.4                   | 0.5      | <0.5    | 11634         | 610            |
| Sewage Sludge | 19.4      | 64.3                   | 0.5      | <0.5    | 1652          | 1725           |
| MSW           | 6–25      | 12–40                  | 0.45–1.0 | <0.5    | 60–200        | 40–100         |

## 2.2 Biomass- and waste-fired boilers

Multiple factors influence the design and construction of the boilers in CHP plants. These factors include the operating temperature, pressure, capacity, and fuel type. The main types of boilers used for biomass and waste combustion are moving grate furnaces and fluidised beds.

### Moving grate furnaces

Figure 2.2 depicts a moving grate-firing system at Avedøre power plant in Denmark. In this system, a biomass or waste feedstock is fed above the grate using a rotary rake system. The grate then moves with a specific motion to ensure appropriate mixing of the fuel. Pre-heated primary air is supplied from beneath the grate to drive the ignition of the fuel. To ensure complete combustion of the organic material and to reduce emissions, excess air is supplied in the secondary air supply system through air nozzles that are situated above the grate. The resulting ash is removed at the bottom through a vibrating motion of the grate. Grate-fired boilers have high levels of efficiency and can be used for the combustion of diverse biofuels. [33]

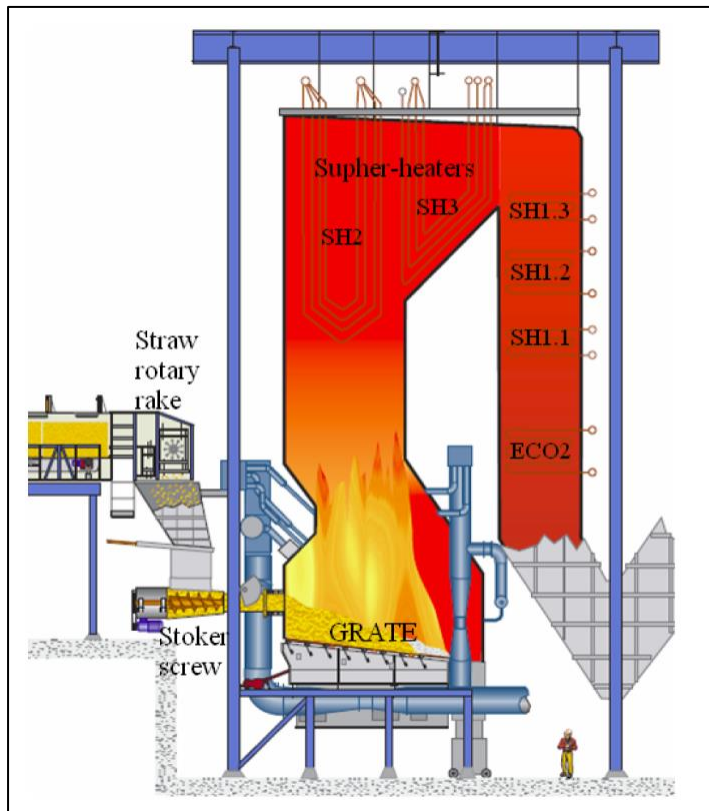


Figure 2.2: Moving grate boiler at Avedøre power plant [33].

## Fluidized Bed Combustion (FBC)

The fluidised bed combustion (FBC) technology uses a bed material, e.g., natural sand that becomes fluidised when air is passed through it at high velocity. In this system, fuel particles are suspended on hot bed materials under pressurised air that is supplied from beneath (primary air duct) and from the side (secondary air duct) (Figure 2.3). In general, there are two types of FBC boilers, namely, circulating fluidised bed boilers (CFB) and bubbling fluidised bed boilers (BFB). The advantage of CFB over BFB is its high efficiency, as the unburned fuel particles can be re-circulated into the combustion chamber for further combustion. Currently, most of the large CHP plants are based on the CFB technology.

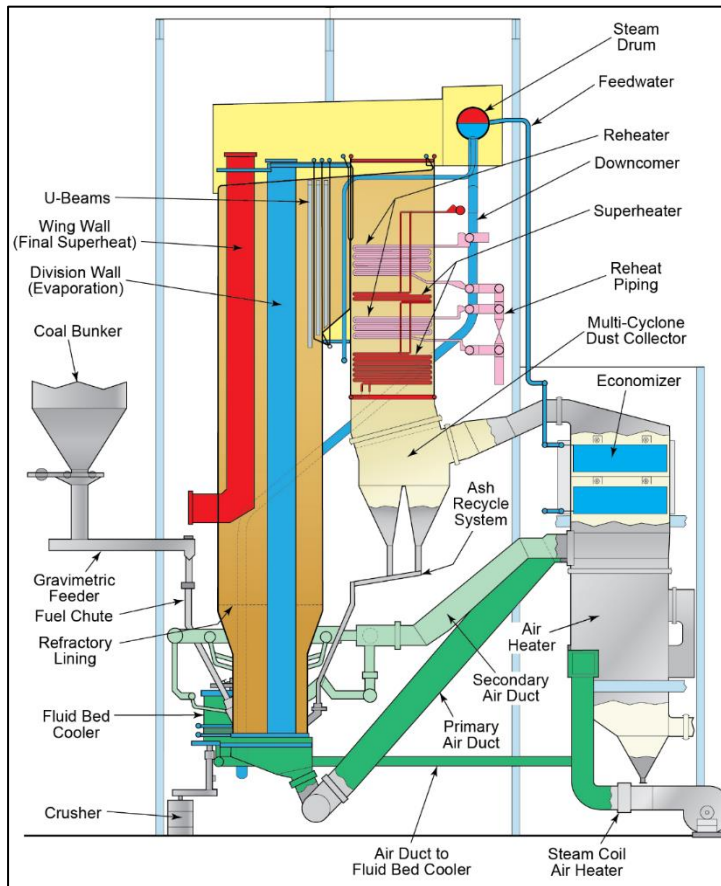


Figure 2.3: Fluidised Bed boiler. Courtesy of The Babcock & Wilcox Company [34]

In comparison to the moving grate boiler, a CFB boiler ensures better mixing of the fuel, which results in high combustion efficiencies. Stringent control of the temperatures across the heating chamber makes it possible to burn out fuels with challenging characteristics, such as high moisture content and high ignition values. However, the main disadvantage of the FBC technology is its sensitivity to fuels that can cause agglomeration of the bed. Bed materials such as natural sand can interact with alkali species in the fuel to form molten alkali aluminosilicate and alkali silicate compounds that stick to the bed particles and cause agglomeration. The problem of bed agglomeration may be mitigated by using more-suitable bed materials. For example, in a study that investigated the interactions between ash components and bed materials, it has been reported that bed agglomeration can be reduced by using ilmenite, which effectively captures alkali species during fuel combustion [35].

### 3. Materials

Alloy is a term that is used to describe a metallic substance that comprises several elements that form a compound. An alloy can be classified according to its content of alloying elements or the type of oxide scales that it forms upon exposure to an oxidising environment. In the development of high-temperature alloys, it is essential to consider the corrosion properties of the alloy. Enhanced corrosion resistance increases material life-time. In addition, the material mechanical properties, such as tensile strength, creep strength should be taken into consideration. During alloy production, different elements, such as molybdenum, tungsten, cobalt, and nickel, may be added to improve corrosion and/or mechanical properties.

#### 3.1 Alloy classification based on content of alloying elements

**Low-alloy steels** contain small amounts of alloying elements. Typically, these alloys contain less than 2.5 wt% chromium [36]. Low-alloy steels usually exhibit good mechanical properties and can be used as load bearers, for example in steam boilers and water walls. However, in alkali-rich environments and at high temperatures, these materials may suffer accelerated corrosion, which shortens their life-times.

**Stainless steels** must contain at least 10.5 wt% chromium and a maximum of 1.2 wt% C [37]. The high chromium content contributes to the formation of a chromium-rich scale, which slows down the diffusion of ions into the alloy and, thereby, resulting in low oxidation of the metal.

**High-alloy steels** contain more than 45% iron, and the total mass fraction of alloying elements is no less than 10% by top limit and mass fraction of one of the elements is no less than 8% by bottom limit [38]. The high-alloy steels typically contain high content of chromium which may form protective chromium-rich oxide scales or chromia, both of which improve their corrosion resistance.

**Nickel-based alloys** typically contain nickel as the principal element. Nickel-based alloys have a wide range of industrial applications due to their high corrosion resistances, advantageous mechanical properties, and low coefficients of expansion. Different alloying elements, such as chromium, molybdenum, copper, titanium, aluminium, and cobalt, may be incorporated into the alloy matrix to ensure specific properties. In general, nickel-based alloys are much more expensive than the previously described alloy classes. Despite their high cost, many of these materials, such as Alloy 625, Alloy 600 and Alloy 800, are employed as components in regions of the boiler that experience severe corrosion and erosion, e.g., the super-heaters and loop seals.

For high-temperature applications where there is high risk of accelerated corrosion (such as in biomass- and waste-fired boiler environments), the use of steels with improved corrosion resistance properties is desirable. To enhance material performance, a high-temperature corrosion-resistant alloy may be applied as a coating on a material that has good mechanical properties.

#### 3.2 Alloy classification based on scale formation.

##### 3.2.1 Chromia-forming alloys

Chromia-forming alloys are alloys that are able to form a chromium-rich oxide scale,  $(\text{Fe,Cr})_2\text{O}_3$  or  $\text{Cr}_2\text{O}_3$ , during oxidation. The formation of chromia requires that the alloy has a sufficient amount of chromium in the alloy matrix to facilitate the formation of such a scale on

the surface. Stainless steels (>10.5 wt% Cr) may form  $(\text{Fe,Cr})_2\text{O}_3$  at the intermediate temperatures relevant to boiler operations ( $\sim 600^\circ\text{C}$ ).

#### Martensitic stainless steels:

These Fe-Cr-C steels are produced by rapidly cooling down (quenching) austenite, whereby carbon gets trapped in the iron lattice and martensite is created. During the quenching process, the face-centred cubic (FCC) structure is transformed into a body-centred tetragonal (BCT) structure. Martensitic steels possess good mechanical properties, such as high creep strength, tensile strength, and toughness. However, they exhibit lower levels of corrosion resistance compared with the other classes of stainless steels.

#### Ferritic stainless steels

Ferritic stainless steels have the BCC structure and contain chromium in the concentration range of 10.5–30 wt%, with very little or no nickel. These steels exhibit good corrosion resistance in aggressive environments. However, they possess enhanced mechanical properties, such as high yield strength, which are desirable for the boiler components, e.g., super-heater tubes.

#### Austenitic stainless steels:

Typically, austenitic stainless steels contain >18 wt% chromium and >8 wt% nickel. They have the FCC structure. These materials exhibit high levels of corrosion resistance in several harsh environments. In addition, this steel class exhibits other desirable properties, such as high weldability (which makes it easy to apply them as a coating), and improved strength and creep resistance (desirable for high-temperature applications).

#### Nickel-based alloys:

Nickel-based alloys have the FCC structure. These alloys contain nickel as the principal element (range, 35–80 wt%). These alloys exhibit enhanced corrosion resistance and good mechanical properties and can be applied in various aggressive environments or in high-temperature systems.

#### 3.2.2 Alumina-forming alloys

##### Ferritic steels

Ferritic steels have the BCC structure. It is well-established that FeCrAl alloys form protective alumina scales at temperatures  $>900^\circ\text{C}$ . However, alumina formation has also been reported at lower temperatures [39]. In other studies, it has been shown that the corrosion behaviours of FeCrAl alloys at around  $600^\circ\text{C}$  may be improved by the addition of silicon [40–42]. The enhanced high-temperature corrosion resistance at higher temperatures allows for FeCrAl alloys to be used in heating elements, furnaces, and turbine components [43].

### 3.3 Alloys used in this study

In this thesis, materials were investigated both as bulk materials and as coatings applied by overlay welding. Table 5.1 shows the alloys investigated in this thesis.

### 3.3.1. Bulk materials

The martensitic stainless steel SVM12 was studied as a reference material and as a substrate for the overlay weld coatings. This material possesses good mechanical properties (e.g., high creep strength), which are achieved by adding tungsten (1.50–2.50 wt%), niobium (0.02–0.10 wt%), and vanadium (0.15–0.30 wt-%). These additives stabilise the martensitic microstructure when the material is exposed to high temperatures [44]. The martensitic microstructure of SVM12 displayed in Figure 3.1 was generated through heat treatment at 1,100°C for 30 minutes, followed by air cooling. This was followed by tempering treatment at 770°C for 2 hours, and finally by air cooling.

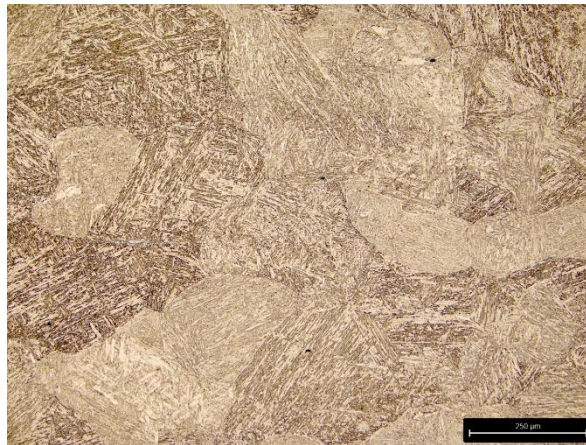


Figure 3.1: SEM image of unexposed martensitic microstructure of the reference material SVM12.

The FeCrAl alloys were studied as bulk and overlay weld versions, so as to compare the corrosion behaviours of these materials and assess their potential applications in harsh environments. Although the abilities of the FeCrAl alloys to form protective  $\alpha$ -alumina scales are reduced at temperatures  $< 900^\circ\text{C}$ , it is still interesting to investigate their corrosion properties at intermediate temperatures relevant to boiler operation (around  $600^\circ\text{C}$ ). The use of FeCrAl alloys, either as composite tubes or overlay weld coatings, would reduce material costs compared to the nickel-based alloys that are currently being used. See Figure 3.2 for a comparison of the material costs.

The chromia-forming alloys (Alloy 27Cr33Ni3Mo and Alloy 625) were studied because they contain high concentrations of chromium, which may form chromium-rich scales that mitigate corrosion in harsh environments. From the mechanical perspective, these alloys contain molybdenum, which has been shown to improve hardness, tensile strength, and elongation to

failure [45,46]. Although nickel-based alloys are expensive, it is worth testing them as they are still used in many boiler parts that are exposed to severe corrosion.

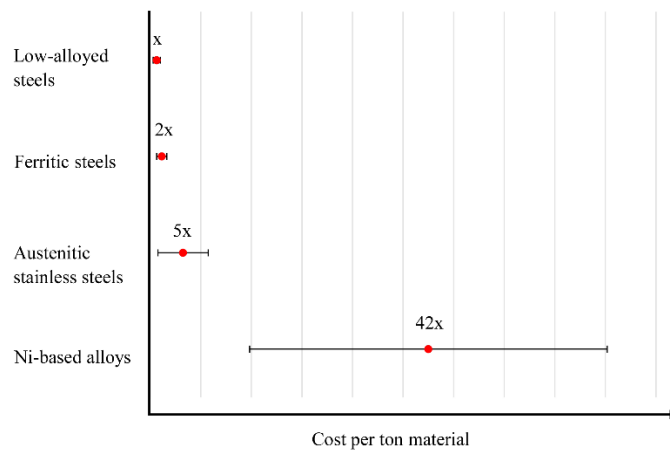


Figure 3.2: Comparison of the costs of the different material classes used as metallic boiler components. The error bars indicate the range of prices within the material class. The term ‘ $x$ ’ is an index of price, as obtained at the time of writing of this thesis [47].

### 3.3.2. Coatings

In harsh environments, such as those experienced in biomass- and waste-fired boilers, the use of corrosion-resistant coatings offers a good alternative for mitigating corrosion that would otherwise reduce the life-times of the metallic components of the boilers. A high-temperature corrosion-resistant coating can be applied onto a cheap, low-alloyed steel that possesses good mechanical properties. This combination improves the life-times of the boiler components and enhances boiler performance. To be successful, a coating must exhibit good adhesion and low porosity, and be compatible with the substrate. Several coating systems have been developed and applied in different parts of the boiler, including:

1. Thermal spray coatings
2. Laser cladded coatings
3. Overlay weld coatings

The thermal spraying technique was first developed in 1882 [48] and was first demonstrated as an effective method to protect steel boiler tubes from high-temperature corrosion in 1937 [49]. Since then, this technique has been developed and can be applied in various ways. Figure 3.3 shows the various thermal spray processes used today to apply coatings, the most common of which are the HVOF and HVAF methods for the application of high-temperature coatings. The principle of the thermal spray technique is that material feedstock is melted in the combustion chamber using a heat source and then accelerated towards a substrate, where it is mechanically bonded. Thermal spraying has several advantages, such as a fine-coating microstructure, low porosity, and low heat input. Generally, the coating thickness is in the micrometre range, although it may also be a few millimetres in thickness depending on the spraying technique used.

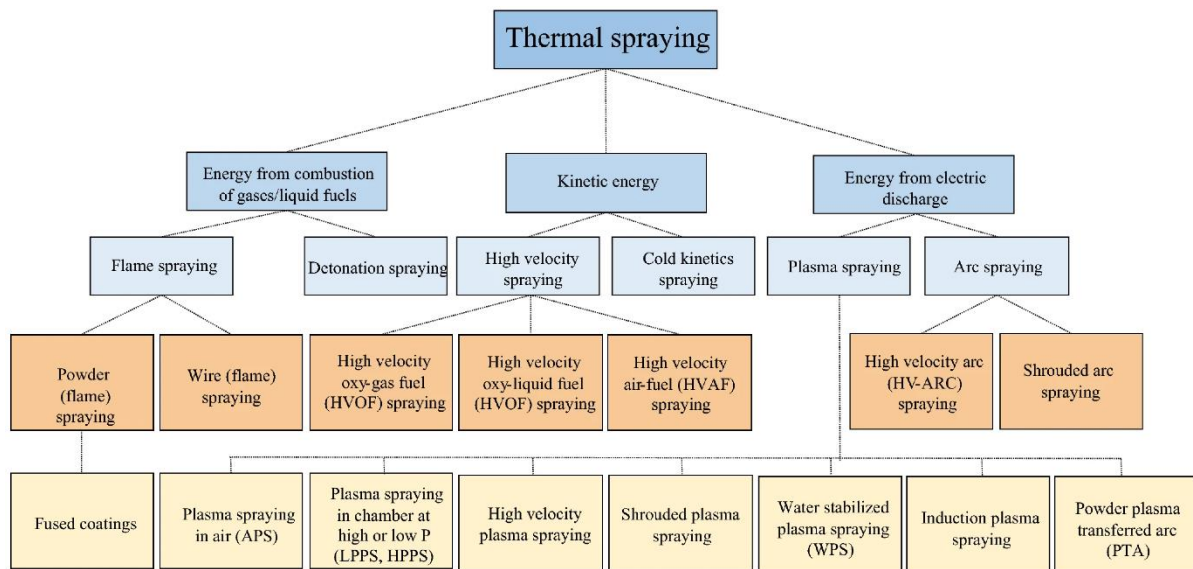


Figure 3.3: Thermal spray techniques [48]

However, it is worth noting that the various thermal spray techniques lead to distinct coating properties. For example, the HVOF technique produces higher quality coatings with low porosity than the HVOF technique, due to the low combustion temperature achieved from the air-fuel mixture.

The laser cladding technique uses the energy of a laser to melt a feedstock and bind it to the substrate. The microstructure of the resulting coating is characterized by low porosity and high adherence to the substrate, with thicknesses in the range of several micrometres to few millimetres. Due to the high impact of the substrate during metallurgical bonding, the risk of dilution is usually high with this technique, and this may affect the mechanical properties of the coating [50].

Overlay welding is another technique that is widely used to produce high-temperature corrosion-resistant coatings. The principle of overlay welding is that a filler material is directly welded onto the substrate. This creates a layered microstructure that is thick and metallurgically bonded to the substrate. Depending on the application, the weld thickness can vary within the range of 6–50 mm. Although overlay welding provides a coating that can withstand harsh environments, dilution and an uneven surface finish can lead to accelerated corrosion of the coating [51]. For application as boiler components (super-heaters), filler materials with corrosion-resistance properties are used, e.g., Ni-based alloys, and the substrate possesses improved mechanical properties, e.g., high creep strength.

In this study, coatings produced through overlay welding were tested for their high-temperature corrosion resistance in a KCl-rich environment. The overlay weld coatings were produced using a mech-MIG with Pulse Multi Control and the technique of Fronius, with built in arc control. The wire (filler material) was melted and re-solidified on the substrate in a single layer, which resulted in coatings with uneven surfaces and with total thicknesses of approximately 7.5–8.5 mm.



## 4. High-temperature corrosion

The high-temperature corrosion (HTC) process involves a chemical reaction that occurs between a metal and its surroundings. This phenomenon concerns materials in processes that are operating at high temperatures, such as gas turbines, heating elements, boilers, mineral processing plants etc. In general, most metals are thermodynamically unstable and will react with oxidising gases in processes such as carburisation, sulphidation, nitridation, and oxidation, leading to the formation of solid reaction products. In this study, the focus is on the high-temperature oxidation of metals.

### 4.1 Oxidation of metals

The process of metal oxidation is of great interest in relation to the design and development of corrosion-resistant materials for applications in severe environments. Oxidation concerns the chemistry between a metal and oxygen to form oxides.

#### 4.1.1 Thermodynamics

The thermodynamics of oxidation of metals allow predictions of which oxides can be formed and under what conditions. For an oxide to be able to form spontaneously, the total free energy of the products must be greater than the total free energy of the reactants. This is the Gibbs free energy ( $\Delta G$ ). For example, consider the reaction in [(Eq. (4.1))] that involves metal  $M$  and oxygen. In this system, the formation of the product ( $MO$ ) will only proceed if there is a negative Gibbs free energy. The reaction will continue as long as there is supply of  $M$  and the  $\Delta G$  value remains negative.



For every alloying element,  $\Delta G$  can be calculated at different oxygen partial pressures and temperatures, and plots of  $\Delta G$  versus temperature can be constructed for each individual oxide and represented in a graph, i.e., an Ellingham diagram (Figure 4.1). This diagram shows the stability levels of the various oxides. At a particular temperature, oxides closer to the top are less stable than the oxides that are lower down. For example, at 600°C (red line),  $Al_2O_3$  lies below  $Cr_2O_3$ , which means that  $Al_2O_3$  is more thermodynamically stable than  $Cr_2O_3$ .

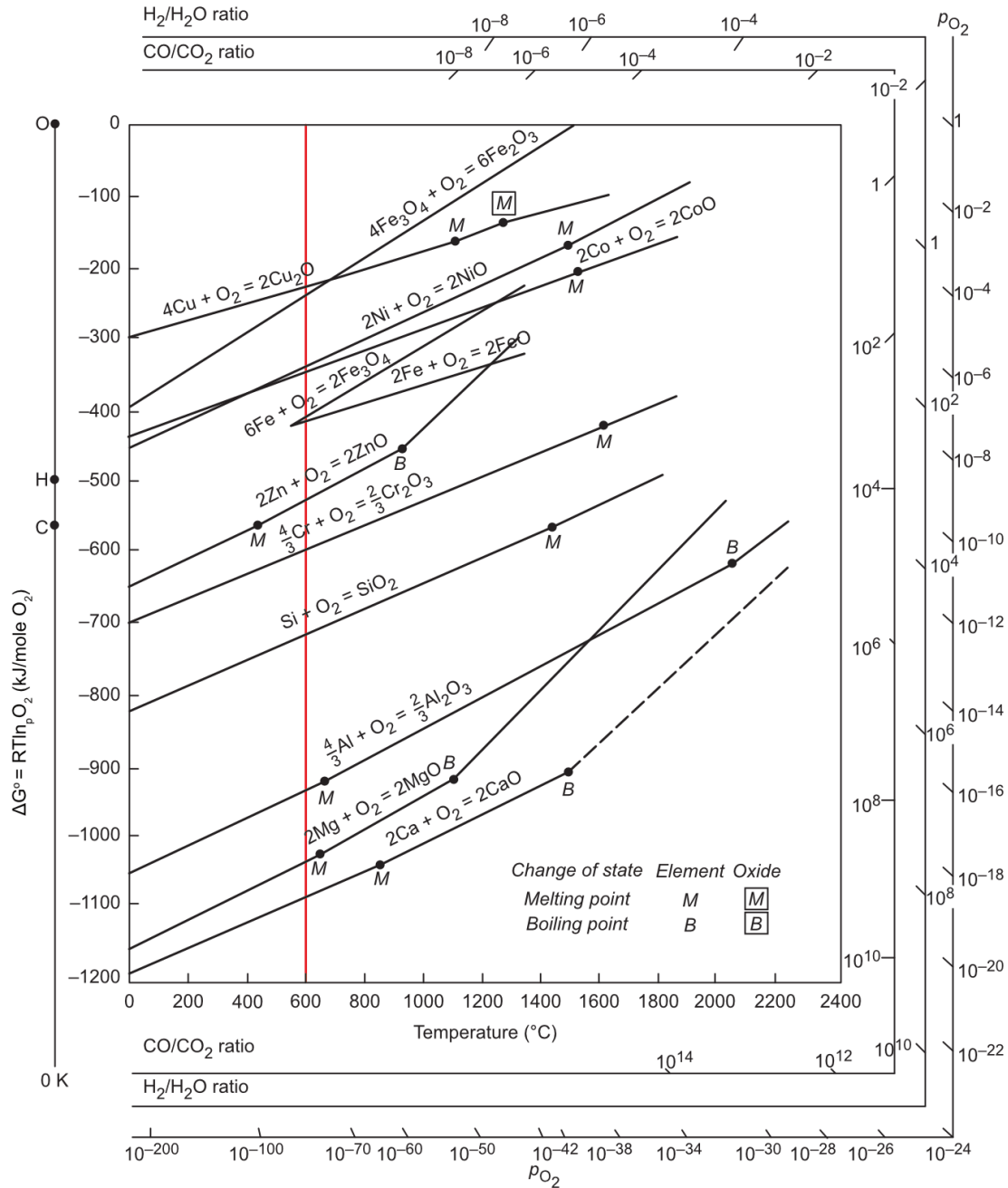


Figure 4.1: Ellingham diagram of free energy versus temperature for some elements. The diagram is adapted from [52].

In alloy design and development, thermodynamic equilibrium calculations can be used to predict the concentrations of alloying elements that are required for certain phases to form at given oxygen partial pressures. In addition, equilibrium calculations are useful for understanding the oxidation processes of coatings where inter-diffusion of alloying elements from the substrate is expected. In a recent study, Bigdeli et al. [53] have described new strategies for modelling the HTC of iron-based alloys using the Calphad Approach. That study reported different decomposition temperatures for the protective corundum structure of the sub-systems: Fe-Al-O, Fe-Cr-O, and Cr-Al-O.

#### 4.1.2 Kinetics

The kinetics of oxidation concerns the mobility of species through the scale and the overall growth behaviours of the oxide scales. Already in the early 20<sup>th</sup> Century, several theories and mechanisms were proposed to explain the processes of scale formation and transportation of

species through the scale. These theories were summarised by Mott and Cabrera [54]. During the initial stages of oxidation, the scale follows a linear rate law [(Eq. 4.2)], which suggests that the rate-limiting step is the adsorption of oxygen at the metal-scale interface:

$$X = k_l * t \quad (\text{eq. 4.2})$$

where  $X$  is the scale thickness,  $k_l$  is the linear rate constant,  $t$  is the time.

The linear law is mostly valid for thin films and the oxidation rate is proportional to time.

However, as the scale thickness increases, the diffusion of ions through the scale becomes significant. Wagner [55] has proposed that the oxidation kinetics in thick scales is governed by the diffusion of cations and anions across the scale and follows a parabolic law [Eq. (4.3)]. Ions diffuse through defective metal sites, such as grain boundaries and dislocations, through a vacancy diffusion mechanism that is driven by the vacancy concentration gradient. In the case of alloys that contain various alloying elements, the growth of the scale follows a diffusion-controlled process which is determined by the diffusivity of the different cations through the scale.

$$X^2 = k_p * t + C \quad (\text{eq. 4.3})$$

where  $k_p$  is the parabolic rate constant, and  $C$  is the integration factor.

Wagner's model assumes that:

- The growing scale is compact and well-adherent to the metal surface;
- The rate-controlling process is the diffusion of ions and electrons through the scale;
- The thermodynamic equilibrium is established at the metal/scale and scale/gas interfaces; and
- The solubility of oxygen is negligible.

Scale growth kinetics is also governed by the logarithmic law, which states that scale growth is faster at the start and decreases rapidly with time. This law applies to thin films at lower temperatures (<300°C) [56]. This behaviour is represented by [(Eq. 4.4)].

$$X = k_{log}(t + t_0) + C \quad (\text{eq. 4.4})$$

where  $X$  is the scale thickness,  $k_{log}$  is the logarithmic constant,  $t$  is time, and  $C$  is a constant.

During long exposures, especially in severe environments, the rate laws described above are not strictly followed, since the thick scale may experience spallation and cracking, in which case the oxidation kinetics becomes a combination of these laws. Breakaway oxidation is a phenomenon that leads to transformation under corrosion regimes. During this process, the scale experiences enhanced growth and transforms from a slow-growing and protective scale (primary protection) to a fast-growing and less-protective scale (secondary protection). Such rapid oxidation kinetics may be explained by some combination of laws, e.g., parabolic-linear growth or logarithmic-parabolic growth.

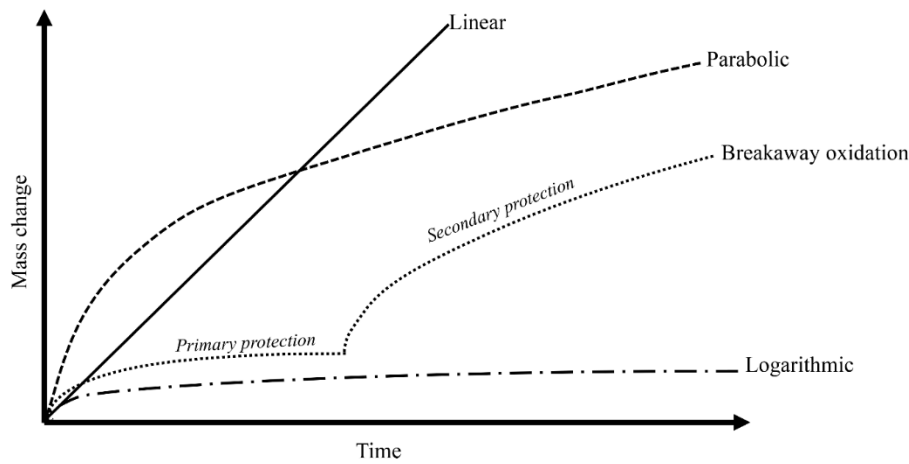


Figure 4.1: Different laws for oxidation kinetics.

## 4.2 Corrosion regimes

Corrosion protection in this context refers to an oxide scale on the metal surface that acts as a barrier between the metal surface and the external environment. During oxidation/corrosion, the metal may exist in different corrosion-protection modes (also known as ‘corrosion regimes’), i.e., primary protection and secondary protection. These concepts were introduced by [57,58] to expand knowledge within HTC and facilitated the study and simulation of the corrosion behaviours of different alloys after breakaway oxidation. These corrosion-protection modes are described further in the following sections.

### 4.1.1 Primary protection

High-temperature alloys rely on the formation of protective scales to defend against any corrosive species. Depending on the alloying elements, which include Fe, Co, Ni, Cr, Mo, Si, and Al, the alloy can form oxides with different corrosion properties. Cr and Al form chromia ( $\text{Cr}_2\text{O}_3$ ) and alumina ( $\text{Al}_2\text{O}_3$ ), respectively, which are thermodynamically stable and protective because they allow only slow diffusion of ions at high temperatures. For this reason, chromia- and alumina-forming alloys are developed for high-temperature applications.

The growth and protectiveness of  $\text{Cr}_2\text{O}_3$  and  $\text{Al}_2\text{O}_3$  at different temperatures and in different environments are of interest to many corrosion scientists. During exposure, the alloy undergoes transient oxidation, whereby solid solutions and simple mixed oxides are initially formed, which then transform into single-phase continuous layers [59,60]. Alloys that contain high levels of chromium quickly form the dense  $\text{Cr}_2\text{O}_3$  scale and can maintain this scale, as there is a constant supply of chromium to the metal-scale interface. However, the stability and protectiveness of  $\text{Cr}_2\text{O}_3$  are limited to temperatures  $<1,000^\circ\text{C}$  due to the volatilisation of  $\text{Cr}_2\text{O}_3$  to gaseous  $\text{CrO}_3$  [61].

For alumina-forming alloys, the protective  $\alpha\text{-Al}_2\text{O}_3$  is normally formed at temperatures  $>900^\circ\text{C}$  [62], although it has also been reported to form at  $700^\circ\text{C}$  [39]. Below these temperatures, it is mainly the metastable alumina phases ( $\gamma\text{-Al}_2\text{O}_3$ ,  $\theta\text{-Al}_2\text{O}_3$  and  $\delta\text{-Al}_2\text{O}_3$ ) that are formed [63]. These transient  $\text{Al}_2\text{O}_3$  variants offer lower levels of protection compared to the  $\alpha\text{-Al}_2\text{O}_3$  variant.

### 4.1.2 Breakaway oxidation

The  $\text{Cr}_2\text{O}_3$  and  $\text{Al}_2\text{O}_3$  scales remain protective at given temperatures as long as structural stability is maintained. However, during exposure in aggressive environments, such as those

found in biomass-fired and waste-fired boilers, these scales rapidly undergo a transformation in which the oxide chemical composition is altered, leading to the formation of a fast-growing and less-protective scale. This type of scale transformation is known as ‘breakaway oxidation’ (separating primary and secondary regimes). Oxidation processes that involve breakaway oxidation exhibit changes in oxidation kinetics, e.g., rapid increase in mass gain, fast growth of oxide scales, and excessive metal loss. Various explanations have been put forward in the literature for the occurrence of breakaway oxidation. One of these is the inability of the alloy to supply sufficient alloying elements, e.g., chromium, to the corrosion front to form and maintain the protective scale. Evidence for this is provided by the rapid oxidation of low-alloyed steels upon exposure to KCl and water vapour [62] as well as Cr-evaporation from the  $\text{Cr}_2\text{O}_3$  scale [64].

#### 4.1.3 Secondary protection

Secondary protection refers to the corrosion regime after breakaway oxidation. The scales formed during this corrosion regime generate more-complex microstructures and normally exhibit enhanced oxidation kinetics. Since different metals have different affinities for oxygen and have different mobilities through the different oxide phases, the resulting scales are multi-layered, often consisting of an outward-growing scale and an inward-growing scale [19,57,65]. The interface between these layers has been interpreted as the original metal-scale interface before breakaway. The direction of scale growth is determined by the direction of ion diffusion through the scale, i.e., the outward-growing scale results from outward diffusion of cations, while the inward-growing scale results from inward-diffusion of anions, as illustrated in Figure 4.2. The position of each oxide in the scale is determined by the stability of the individual oxide along the oxygen partial pressure gradient (see Ellingham diagram in Figure 4.1).

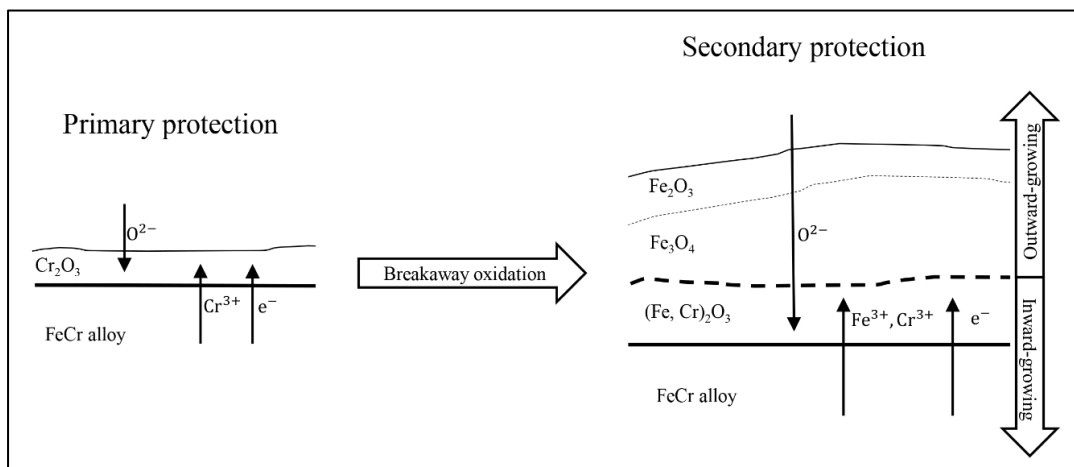


Figure 4.2: Schematic of the different corrosion protection modes for a chromia-forming alloy.

At  $600^\circ\text{C}$  (temperature relevant for boiler application), alloys exhibit different corrosion behaviours within the secondary corrosion regime. This means that the formed oxide scales exhibit varying degrees of corrosion resistance. Upon exposure to harsh environments, low-alloyed steels form fast-growing Fe-rich oxide scales that consist of hematite ( $\text{Fe}_2\text{O}_3$ ), magnetite ( $\text{Fe}_3\text{O}_4$ ) and, in some cases, wüstite ( $\text{FeO}$ ) in the outer scale and iron-chromium spinels in the inner scale [57,66]. Iron-based chromia- and alumina-forming alloys form Fe-rich oxide scales in the outer scale and Cr-rich spinel in the inner scale. The sequence of oxide formation is dictated by the different mobility rates of the cations through the defects of the

spinel, with  $\text{Fe}^{2+}/\text{Fe}^{3+}$  exhibiting faster mobility than  $\text{Cr}^{3+}$  [67,68]. The addition of other alloying elements, such as Si, has been reported to promote the formation of a more Cr-rich inward-growing scale that exhibits a more-protective behaviour [69,70].

The concept of secondary corrosion protection becomes more relevant for materials that are exposed to harsh conditions for long operational times at intermediate temperatures ( $\sim 600^\circ\text{C}$ ). The oxide microstructures formed after breakaway determine the life-time of the material. This thesis contributes with insights into the long-term corrosion behaviours of high-temperature alloys in harsh environments.

### 4.3 Corrosion mechanisms

Several factors contribute to the oxidation process of metals, e.g., environment and temperature. Depending on the environment, the metal undergoes different corrosion mechanisms, whereby the alloying elements interact with the corrosive species in the environment. Studies of corrosion mechanisms have traditionally focused on the initial stages of oxidation or short-term corrosion process, i.e., within the primary corrosion regime. This thesis focuses on the corrosion behaviour after breakaway (secondary corrosion regime).

In the following sections, the most-common HTC mechanisms in environments created during the combustion of biomass/waste will be described.

#### 4.2.1 Chlorine-induced corrosion – “Chlorine cycle”

The chlorine-induced corrosion mechanisms initially proposed by McNallan et al. [71] and further developed by Grabke [72] attribute a catalytic role to chlorine in the oxidation process of metals. This mechanism follows three steps: initiation, propagation, and termination. In the initiation step, chlorine is released from chlorine-containing species, e.g., through the oxidation of HCl [(Eq. 4.5)]. The formed chlorine gas is then transported through the protective oxide scale and reacts with the alloying element, leading to the formation of volatile metal chloride at the scale-metal interface, according to [(Eq. (4.6))]. Since the oxygen partial pressure is higher at the scale-gas interface than at the metal-scale interface, a driving force is created that causes the volatile metal chloride to diffuse outwards through the porous scale. Upon reaching regions with higher oxygen partial pressures, the metal chloride is converted into its oxide, according to [(Eq. (4.7))]. This final step also leads to the release of chlorine, which either evaporates or is transported back to the metal-scale interface, such that the cycle repeats.

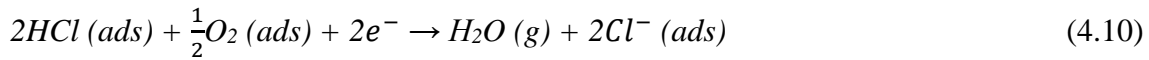


During combustion of biomass/waste, chlorine is released from the alkali chlorides and HCl that are present in the flue gas.

Although active oxidation is a widely accepted corrosion mechanism, some scholars have questioned the likelihood that molecular chlorine (396 pm) diffuses through a scale that is otherwise impenetrable to molecular oxygen (264 pm). For this reason, a different mechanism based on electrochemical process has been put forward.

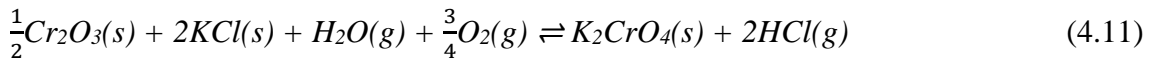
#### 4.2.4 Chlorine-induced corrosion – “Electrochemical approach”

The electrochemical approach suggested by Folkesson et al. [73], involves a redox reaction in which molecular chlorine dissociates at the scale-gas interface to form chloride ions [Eq. (4.8)]. Simultaneously, cations are created at the metal-scale interface via oxidation [Eq. (4.9)], and this provides an electron current. In the case of biomass combustion, where there is a high HCl content, chloride ions are released via deprotonation of HCl, according to Eq. (4.10), and reduction of oxygen at the cathode.



#### 4.2.2 Chromate formation

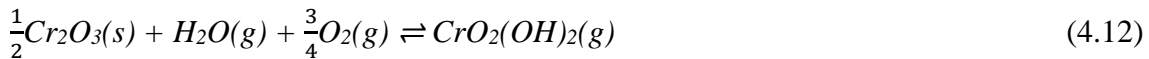
This mechanism involves the formation of alkali chromate, which depletes the scale of chromium and, consequently, impairs its protective properties. Pettersson et al. [7] have proposed that alkali chloride species, e.g., KCl, react with the protective scale ( $Cr_2O_3$ ) to form alkali chromate and release HCl, according to [(Eq. 4.11)]. The presence of chromate has been reported in several studies [74,75].



The formation of chromate is undesirable, as it continuously reduces the amount of chromium that would otherwise form the protective scale. In environments that are rich in alkali species, such as those in biomass- and waste-fired boilers, accelerated corrosion due to continuous chromate formation reduces the life-time of the material.

#### 4.2.3 Chromic acid formation

Water vapour acts as an aggressive species that destroys the protective chromia layer, according to [(Eq. (4.12))], leading to the formation of chromic acid ( $CrO_2(OH)_2$ ) [64]. The effect of water vapour on the corrosion of metals has been investigated in many studies [76,77]. It has been suggested that the formed chromic acid is removed through evaporation, which constantly shifts the equilibrium of the reaction to the right. This results in continuous depletion of the scale for Cr. The processes of chromic formation and evaporation lead to breakaway oxidation, whereby the protective scale is destroyed and a poorly protective scale is formed.



Other studies have attributed the effect of water vapour on metal oxidation to its involvement in reactions at the metal surface that change the oxidation mechanism [78,79]. These studies suggest that  $H_2O(g)$  is the main source of oxygen and that it promotes internal oxidation of Cr in FeCr alloys.



## 5. Experimental section

The experimental procedures are described in two parts: *Set-up development* and *Corrosion exposure*, as shown in Figure 5.1. The order of performance is indicated by the numbers in the figure.

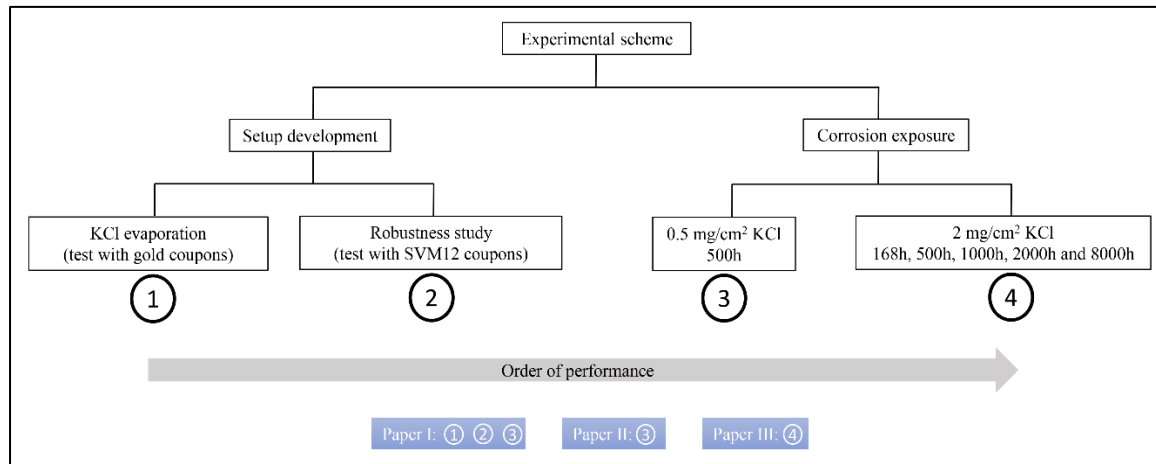


Figure 5.1: Flow chart showing the different experimental activities carried out in this thesis in the order of 1, 2, 3 and 4.

### 5.1 Set-up development

#### 5.1.1 KCl evaporation

In this work, an experimental set-up was developed and optimised that minimises KCl evaporation so as to enable long-term corrosion testing with salt on sample surfaces at 600°C. For this purpose, KCl evaporation tests were performed using three (24-carat) gold coupons. The effect of gas flow on KCl evaporation was investigated by testing two gas flows: 0.1 cm/s and 0.5 cm/s. In addition, a large KCl source (KCl boat) was placed up-stream of the samples to saturate the incoming gas with KCl before passing over the samples. Prior to exposure, the gold samples were sprayed with varying amounts of KCl (range, 0.2–0.9 mg/cm²). The samples were then left to dry in a desiccator for 24 hours and re-weighed before exposure. The gold samples were then exposed to an environment that consisted of 5% O<sub>2</sub> + 20% H<sub>2</sub>O + N<sub>2</sub> (Bal) in a three-heating-zone silica tube furnace (Figure 5.2). The temperature in all three heating zones was set to 600°C and calibrated using a thermocouple type K, allowing a heating zone of about 11 cm (Figure 5.3).

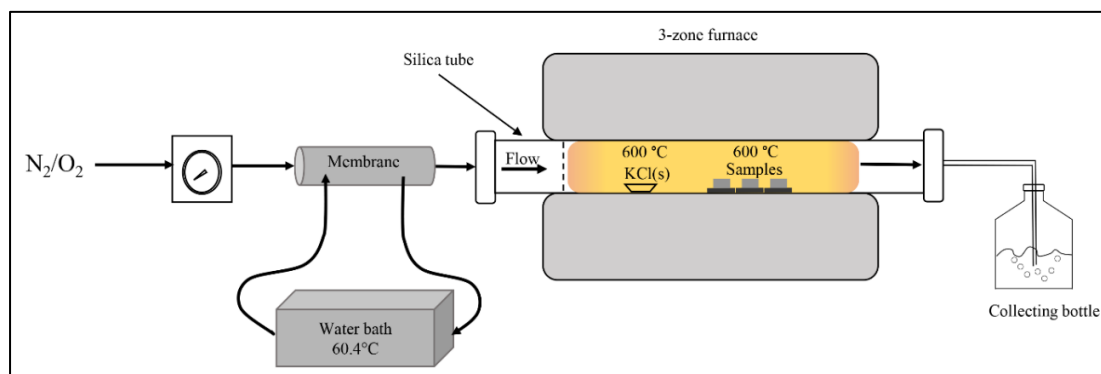


Figure 5.2: Schematic of the experimental set-up used for the investigations in this thesis.

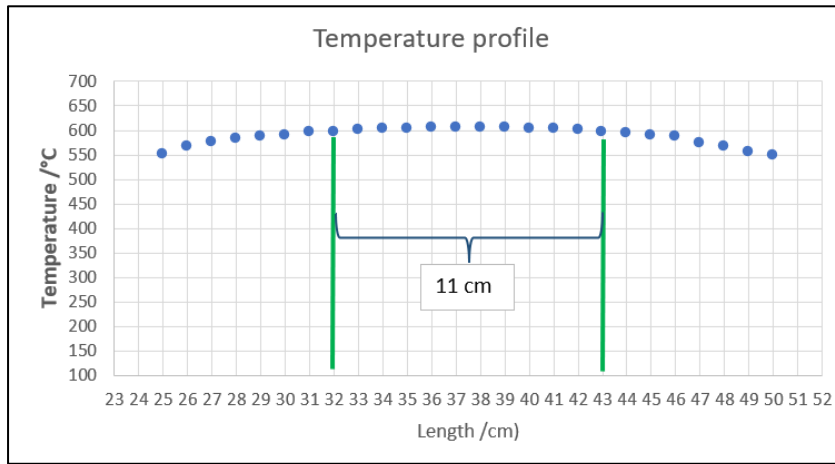


Figure 5.3: Temperature profile in the three-heating-zone furnace used for exposures in this study.

### 5.1.2 Robustness study

In order to validate the robustness of the set-up, a 168-hour exposure was carried out using 18 coupons of the reference material (SVM12). The coupons were prepared by grinding the flat surfaces with 800 grit SiC paper and the edges with 500 grit SiC paper. The samples were then de-greased using an ultrasonic bath that contained acetone, followed by cleaning with ethanol. KCl salt was pre-deposited onto the samples by spraying a solution that consisted of 80 vol% ethanol and 20 vol% distilled water saturated with KCl. During spraying, warm air was passed over the samples to enable faster drying of the salt. Samples were weighed in between the spraying, to ensure that the desired amount of KCl was deposited. The samples were then incubated in a desiccator for 24 hours and re-weighed just before exposure.

## 5.2 Long-term exposures

### 5.2.1 Materials

The secondary protective properties of alumina- and chromia-forming alloys after long-term exposures were investigated using the newly developed set-up described in Section 5.1. In addition, the alloys were studied as bulk as well as overlay weld coatings to compare their corrosion performances. Table 5.1 and Table 5.2 show the tested versions and chemical compositions, respectively. The newly developed martensitic stainless steel SVM12 was supplied by Vallourec SA and tested as the reference material and as the substrate for the overlay weld coatings. The ferritic steels (FeCrAl) were supplied by Kanthal AB. The austenitic stainless steel 27Cr33Ni3Mo and the nickel-based Alloy 625 were supplied by Alleima AB. The bulk materials were received as coupons with dimensions of 20×10×2 mm, while the overlay weld had the dimensions of 20×10×8 mm. A detailed description of how the overlay welding process was conducted can be found in Section 3.3.2.

Table 5.1: Alloys studied in this thesis.

| Material       | Alloy type                  | Tested as |              |
|----------------|-----------------------------|-----------|--------------|
|                |                             | Bulk      | Overlay weld |
| SVM12          | Martensitic stainless steel | Yes       | No           |
| Kanthal® EF101 | Ferritic steel              | Yes       | Yes          |
| Kanthal® EF100 | Ferritic steel              | Yes       | Yes          |

|                   |                            |                                     |     |
|-------------------|----------------------------|-------------------------------------|-----|
| APMT              | Ferritic steel             | Yes                                 | Yes |
| Alloy 27Cr33Ni3Mo | Austenitic stainless steel | Yes                                 | No  |
| A625              | Nickel-based alloy         | Yes (in activity 3, see Figure 5.1) | Yes |

Table 5.2: Chemical composition of the alloys studied in this thesis.

| Material          | Chemical composition (wt-%) |      |      |     |       |      |       |      |
|-------------------|-----------------------------|------|------|-----|-------|------|-------|------|
|                   | C                           | Si   | Mn   | Mo  | Cr    | Al   | Ni    | Fe   |
| SVM12             | 0.16                        | 0.6  | 0.8  | 0.6 | 12.0  |      | 0.4   |      |
| Kanthal® EF101    | 0.02                        | 1.25 | 0.10 |     | 12.4  | 3.7  |       | Bal. |
| Kanthal® EF100    | 0.02                        | 0.3  | 0.2  |     | 10.1  | 4.0  | <0.5  | Bal. |
| APMT              | 0.08                        | 0.7  | 0.4  | 3.0 | 21.0  | 5.0  |       | Bal. |
| Alloy 27Cr33Ni3Mo | 0.1                         | 0.8  | 2.0  | 3.0 | 25-31 |      | 27-36 |      |
| A625              | 0.1                         | 0.2  | 0.35 | 9.0 | 21.0  | 0.19 | 63.0  |      |

#### 5.2.2. Sample preparation and exposures

The bulk materials were prepared according to the procedure described in Section 5.1.2 (*Robustness study*). The overlay weld coatings did not undergo any sample preparation.

Two sets of corrosion tests were performed with different amounts of KCl pre-deposited on the samples. In the first set of tests, 0.5 mg/cm<sup>2</sup> KCl was deposited on the samples (both bulk and overlay weld coatings), which were then exposed for 500 hours. In the second set of tests, 2 mg/cm<sup>2</sup> KCl was deposited on the samples (both bulk and coatings), followed by exposures for 168, 500, 1,000, 2,000, and 8,000 hours.



## 6. Analytical techniques

Several analytical techniques were used in this work to characterise the corrosion products and to investigate the microstructural evolution of the scales formed by the different materials and coatings. The various techniques are described in detail in the following sections.

### 6.1 Cross-section preparation - broad ion beam (BIB) milling

Broad ion beam (BIB) milling is a powerful tool for preparing cross-sections for analysis with SEM. Ion milling produces wide and smooth surfaces, making it possible to observe and characterise the minute features of the sample. During the milling process, ions are produced from an ion source (Ar) and accelerated towards the sample surface. As the ions interact with the sample surface, atoms are ejected from the sample surface, resulting in a smooth cross-section. Figure 6.1 shows the difference between an ion-milled region and a mechanically polished region of the same sample. Since the milled section is large, a representative region can be selected for further analysis. In this work, two BIB milling systems were used: the Leica EM TIC 3X for cross-section milling, operated at 8 kV; and the Gatan PECS II system for planar milling, operated at 6 kV.

Prior to milling, the cross-sections are prepared by cutting the samples and polishing (up to 0.5  $\mu\text{m}$ ) using the Leica EM TXP target surfacing system. The sample is then fastened onto the stage behind a mask that protects the sample from direct collision with the incoming beam, and the milling process proceeds in a vacuum.

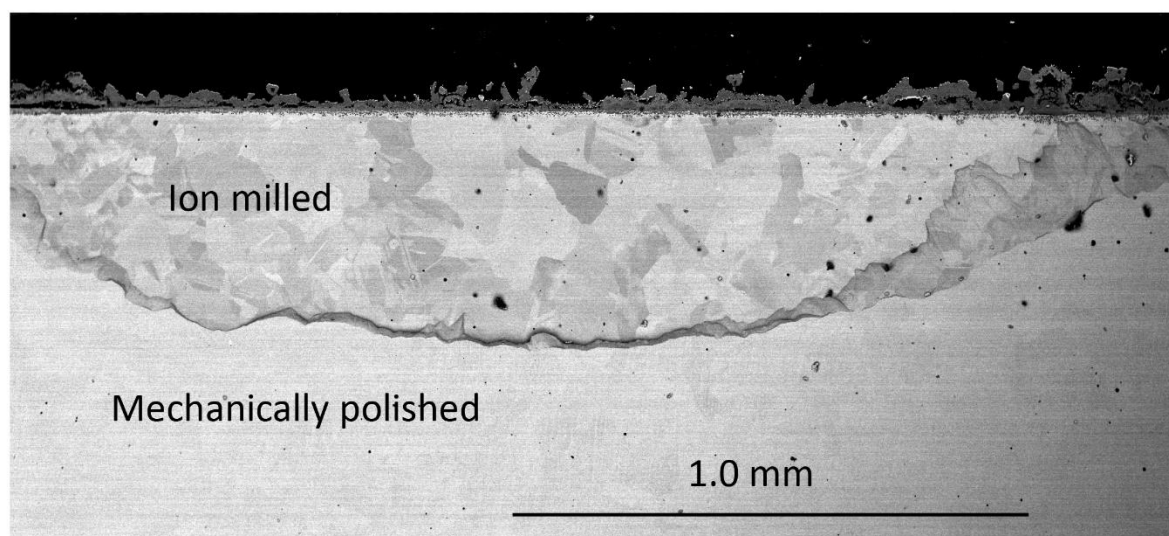


Figure 6.1: Cross-sectional images showing ion-milled and mechanically polished regions of the same sample.

### 6.2 Light Optical microscopy (LOM)

Light optical microscopy (LOM) utilises the ability of the lens to bend photons generated from a light source and focus it on the studied specimen. The resolution of LOM is limited by the wavelength of the visible light, which is in the range of 0.4–0.7  $\mu\text{m}$ . In this study, LOM was used to check the sample surfaces during specimen preparation. In addition, the tool was used to acquire low-magnification images of cross-sections of the samples after exposure to reveal

the oxide thicknesses (Figure 6.2). However, to observe smaller features, a technique with higher spatial resolution, such as scanning electron microscopy (SEM), must be used.

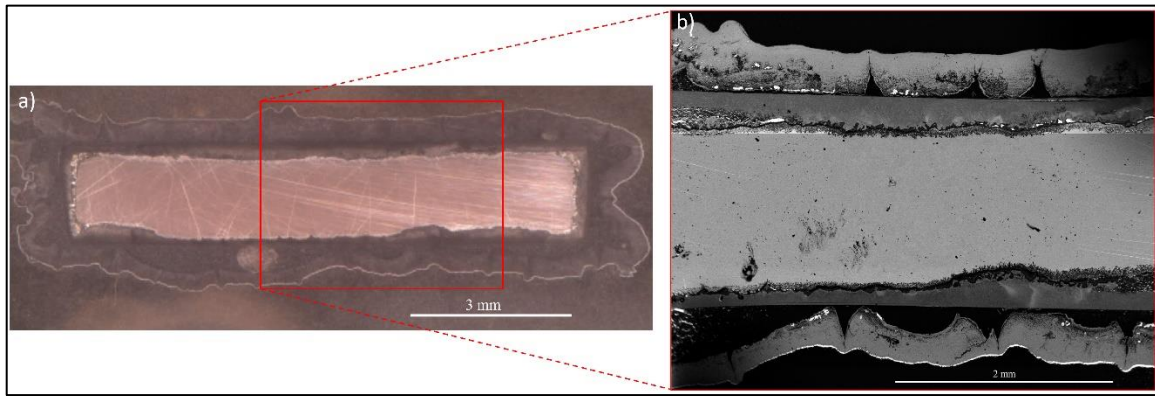


Figure 6.2: Images of the cross-section of a sample after exposure for 2,000 hours. a) Low-magnification image acquired by light optical microscopy, revealing the entire oxide scale. b) High-magnification SEM-BSE image, revealing detailed features of the scale.

### 6.3 Scanning electron microscopy (SEM)

For more-detailed characterisations of corrosion products, the scanning electron microscope (SEM) was used. SEM, which uses electrons to create an image with high spatial resolution, can be used for several purposes, for example, to acquire information about the morphology, topology, chemical composition, and structure. A schematic of SEM instrument is presented in Figure 6.3. The working principle of SEM is that electrons are generated by an electron source (electron gun) at the top and are accelerated to energies in the range of 0.1–30 keV. A system of electro-magnetic lenses converges the electron beam into a narrow probe. The focused beam is then swept across the sample using scanning coils, thereby generating signals that can be converted into images by the detectors.[80]

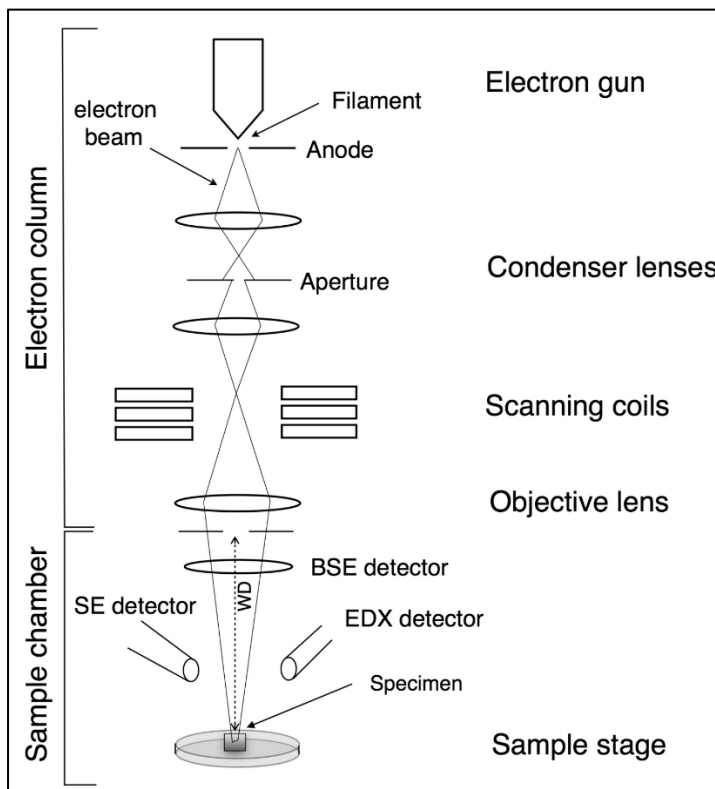


Figure 6.3: Schematic of a scanning electron microscope, showing the different components and optics [80].

Upon interacting with the sample, three types of signals are generated: a) secondary electrons; b) back-scattered electrons; and c) characteristic x-rays. The magnitude of each signal generated reflects the interaction volume, which in turn depends on several other factors, such as the accelerating voltage, type of material, and angle of incidence. Different signals emanate from the sample from different depths, as shown in Figure 6.3. A higher accelerating voltage results in a larger interaction volume and reduced spatial resolution.

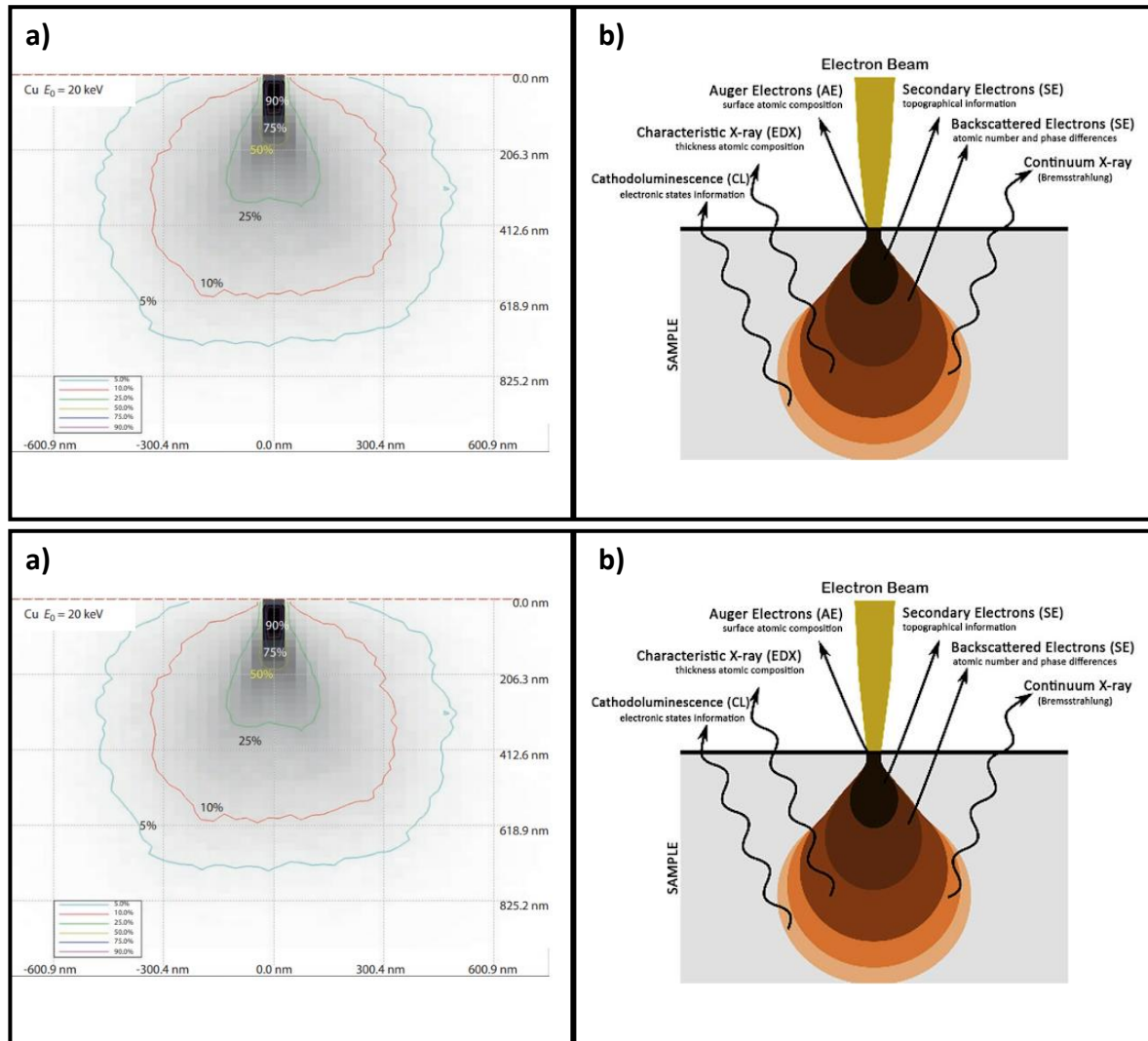


Figure 6.3: Interaction volume depicting the energy disposition when the electron beam interacts with the sample surface. a) Based on a CASINO Monte Carlo simulation and reported by [80]. b) The different signals emitted within the interaction volume.

### Secondary electron (SE)

Secondary electrons are low-energy electrons ( $<50$  eV) that are emitted when the incident beam inelastically interacts with the sample surface. SEs can only escape from regions that are close to the surface, which makes them surface-sensitive. As the electron beam scans across the surface, more SEs are emitted from high-angled areas of the object, giving rise to an edge effect. This enhanced SE escape along the edges can be utilised to obtain information about the topography of the sample.

## **Backscattered electrons (BSE)**

Back-scattered electrons (BSE) are generated from larger interaction volumes, due to the elastic interactions of electrons with the nuclei of atoms in the sample. Atoms with higher atomic numbers or denser regions generate more scattered electrons. During imaging with the BSE detector, regions that contain elements with high atomic numbers/denser regions will appear brighter. This principle can be exploited to acquire information about the composition of the sample. BSE consist of high-energy ( $>50$  eV) particles.

In this work, SEM has been employed as an important tool for the characterisation of the thick oxide scales formed after long exposures. Detailed microstructural analyses of the oxide provide insights into the mechanisms underlying scale formation and growth. These analyses were performed on ion-milled cross-sections using the Environmental Scanning Electron Microscope (ESEM), together with the FEI Quanta 200 SEM. The accelerating voltage was in the range of 8.5–12 kV for imaging with the BSE detector and was 20 kV for the chemical analyses with the EDX detector.

## **Characteristic X-rays**

X-rays escape from deeper regions in the interaction volume (Figure 6.3b). When high-energy primary electrons interact with the inner shells of the atom, electrons are ejected from their original shells, leaving the atom in an excited state with a missing inner shell electron. Upon relaxation, an electron from the outer shell fills the vacant electron position and energy is emitted in the process. The emitted energy is characteristic for the atom involved in the process and gives information about the nature of the element. X-rays are used for both qualitative analyses, i.e., elemental mapping, and quantitative analyses, i.e., elemental content of the sample.

## **6.4 Electron backscatter diffraction (EBSD)**

Electron back-scatter diffraction (EBSD) allows the collection of crystallographic information from the sample in the SEM. In this work, EBSD was used to identify the crystalline phases within the oxide scales and the bulk. The EBSD technique utilises electron channelling contrast imaging with the EBSD detector. The working principle is that the electron beam interacts with a tilted sample and is diffracted by lattice planes from different depths within the sample. Depending on the orientation of the lattice planes, BSEs of varying intensity are detected and captured as images with different grey-scale levels using a CCD camera. The diffraction patterns from the lattice planes of the crystal are represented as electron back-scatter patterns, called Kikuchi bands, on a phosphor screen. Since the arrangement of the Kikuchi bands is a direct projection of the orientation of the lattice planes, they can be indexed to obtain information about the crystalline material, e.g., phases, grain size and texture. An example of the Kikuchi bands for the hematite crystal structure is shown in Figure 6.4. Phase identification in the present work was performed using the TESCAN GAIA3 dual beam instrument operated at 20 kV on ion-milled cross-sections.

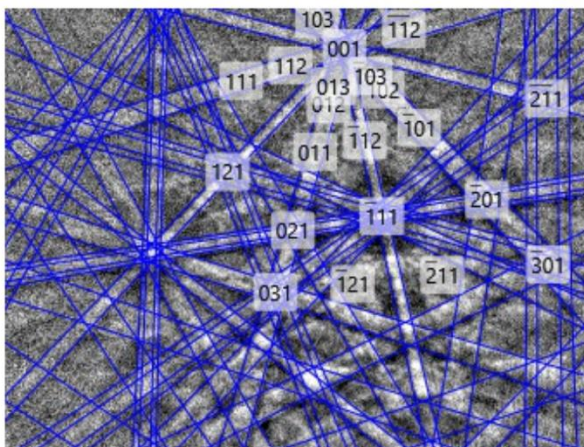


Figure 6.4: Kikuchi bands for the hematite phase

## 6.5 Transmission electron microscopy (TEM)

Transmission electron microscopy offers very high resolution (sub-ångström resolution) and can be used for the imaging and chemical analysis of various materials. The principle of scanning TEM (STEM) is similar to SEM where electro-magnetic lenses are used to focus an electron beam onto a sample surface. In contrast to SEM, the samples to be analysed by STEM must be very thin ( $<100$  nm) [81]. The TEM is operated with high-energy electrons (about 80–300 keV) that go through the sample. For this study, the TEM analysis was performed by Dr. Imran Hanif. The FEI Titan 80–300 STEM equipped with the Titan field emission gun, an Oxford X-sight EDX detector, and high-angle annular dark field (HAADF) detector was used. The instrument was operated at 300 keV. Prior to analysis with STEM, the samples were prepared using a dual-beam Versa 3D Focused Ion Beam (FIB) milling machine to produce thin lamellae. A detailed description of the FIB sample preparation can be found elsewhere [10].

## 6.6 X-ray diffraction (XRD)

XRD is a quantitative and qualitative analytical technique that is used to acquire structural information about a material, such as the crystalline phases and degree of crystallinity. X-ray diffraction is based on constructive interference of an x-ray beam with the crystalline material. The principle of x-ray diffraction is that poly-chromatic x-rays produced in a cathode tube are filtered to obtain a mono-chromatic beam, which then interacts with the lattice planes of the crystalline material. This interaction leads to elastic scattering of the x-ray beam, which upon constructive interference creates a diffraction pattern that can be displayed in a diffractogram (based on positions and intensity). In this thesis, the Bruker D8 Discover diffractometer was used with a Mo radiation source. The Mo radiation source was selected so as to produce more-intense radiation that achieves greater penetration of the thick oxide scales formed by the alloys during long exposures.

## 6.7 Average grain size measurement

The average grain sizes for the oxides formed by the alloys were obtained from SEM-BSE cross-sectional images of milled samples using the average grain intercept (AGI) method described in the ASTM E112-12 standard [82]. In this method, several test lines are drawn over a region of interest, and the number of intersections between the lines and the grain boundaries

is noted. For example, in Figure 6.7, line 1 intersects the grain boundaries seven times (green dots). A similar procedure is performed for all the lines.

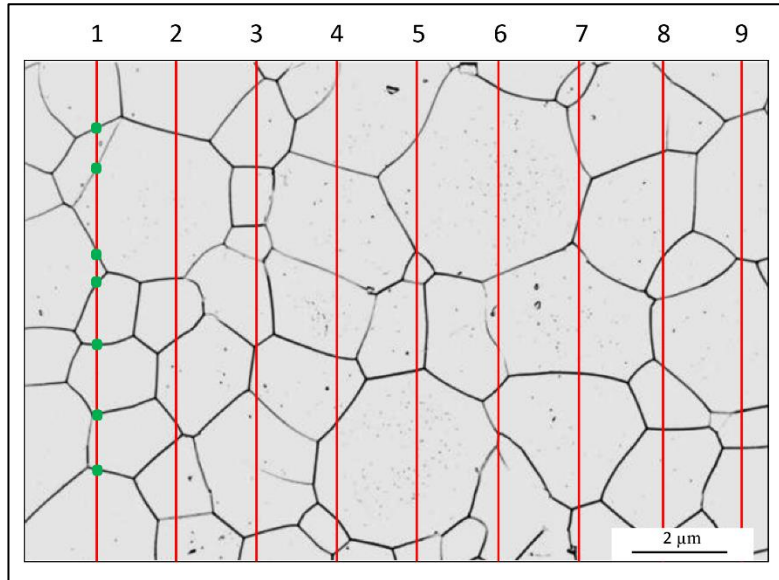


Figure 6.7: The intersect method for determining the average grain sizes for oxides and steels.

The average grain size ( $N$ ) can be calculated using the equation:

$$N = \frac{n \cdot p}{\sum x - 1}$$
 where  $n$  is the number of lines,  $P$  is the length of the test line, and  $X$  is the number of intersects.

## 6.8 Computational modelling and simulation

Thermodynamic equilibrium calculations were performed using the Thermo-Calc software 2023a with the oxide database TCOX12, to calculate the stable oxide phases formed by different alloys. The fraction of stable phases was plotted against the oxygen partial pressure. For the kinetic simulation, the Dictra software in Thermo-Calc was used. The calculations and simulations were performed by Dr. Sedigheh Bigdeli.

## 7. Results and Discussion

The present work investigated the long-term high-temperature corrosion behaviours of materials and coatings for applications in biomass-fired and waste-fired boilers. The first section of this chapter describes the results obtained from the experimental set-up, as well as the initial corrosion tests with the reference material. The second section concerns the results from the long-term corrosion investigations of materials and coatings for boiler application. Since the focus of the study is to understand the corrosion behaviour after long exposure times, the discussion will revolve around the protective properties of the formed oxide scales within the secondary corrosion regime, i.e., after breakaway oxidation.

### 7.1 State-of-the-art exposures for long-term corrosion investigations

#### 7.1.1 Conditions to mimic the boiler environment.

It is well known that the combustion of biomass/waste creates an environment that contains species such as KCl and water vapour, which promote accelerated corrosion of metallic boiler components [7,9]. Investigations of alkali chloride-induced corrosion have shown that this rapid corrosion results in shorter life-times for the materials [57]. Thus, to study the corrosion behaviours of steels used in boiler applications, it is necessary to set up an experimental procedure that mimics the boiler environment and/or contains the key components of the environment from the corrosion perspective. There are several ways to achieve this, and two are considered in this thesis: 1) to test the materials at a higher steam temperature than that used currently, 450°C (steam temperature) [83]; and 2) to select a representative chemical environment that best mimics the corrosive nature of the biomass-fired and waste-fired boilers. It should be noted that the concept of secondary protection/regime is generic and is not limited to the breakaway mechanism/environment.

The experimental temperature used in the work of this thesis was chosen with consideration of the enhancement of electricity efficiency in CHP systems. To obtain the maximum efficiency and have economically viable CHP systems, the steam pressures and temperatures must reach super-critical levels or even ultra-super-critical levels (steam temperature/pressure of ~600°C/>270 bar). Theoretical calculations suggest that raising the outlet steam temperatures to 600°C can result in an electricity efficiency of up to 45% [84,85], as compared to the current efficiency level of 25%–37% [26]. However, raising the steam temperature would lead to an increase in the material temperature to slightly above the steam temperature. These ultra-super-critical operating parameters have not yet been implemented in biomass-fired and waste-fired plants due to the limited availability of materials that can withstand such harsh environments.

Regarding the chemical environment, various studies have shown that KCl and water vapour act aggressively towards boiler steels, given that they induce breakaway oxidation and cause accelerated corrosion. Thus, the investigations in this study were carried out at 600°C in the presence of 5% O<sub>2</sub> + 20% H<sub>2</sub>O + N<sub>2</sub> (Bal) + KCl(s)/KCl(g), to induce breakaway oxidation.

Furthermore, to evaluate the long-term corrosion behaviours of high-temperature alloys in an environment where KCl(s) is present for a prolonged period, a systematic experimental design is required in which the corrosive species are present throughout the exposure. However, a challenge associated with investigations of KCl-induced corrosion is the high evaporation rate of KCl(s) at 600°C. Most previous studies investigating KCl-induced corrosion have been

carried out for short-term exposures, designed to investigate the initiation/breakaway corrosion [8,73,86–88]. The experimental set-up used in this thesis involved pre-deposition of KCl(s) on the samples and a low gas flow rate, in combination with a KCl(s) source placed up-stream of the samples, to reduce the rate of KCl evaporation from the sample surfaces and to ensure the presence of KCl(s) salt on the samples throughout the exposure. The presence of unreacted KCl particles on the surface of the reference material (SVM12) after 168 hours of exposure is shown in Figure 7.1.

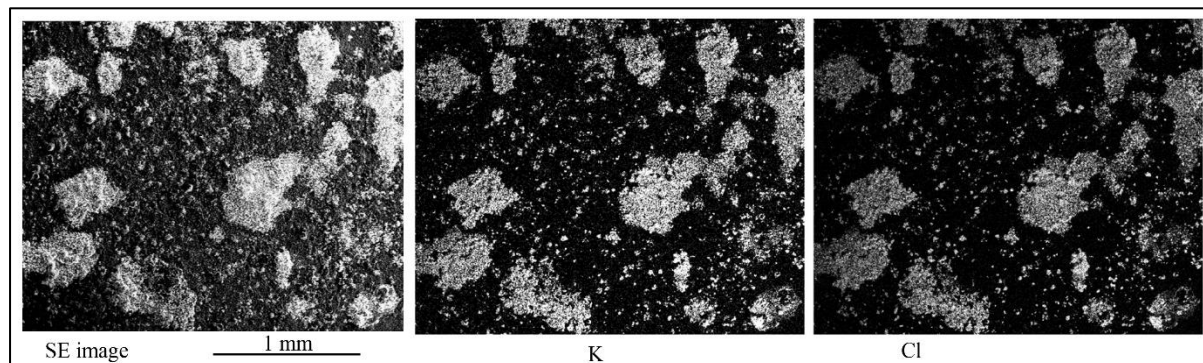


Figure 7.1: SEM image showing the presence of unreacted KCl particles on the reference material, SVM12, after exposure to 5%  $O_2$  + 20%  $H_2O$  +  $N_2$  (Bal) + KCl(s)/KCl(g) for 168 hours.

#### 7.1.2 Robustness of the set-up

The reliability and effectiveness of the experimental set-up were tested by exposing 18 samples of the reference material (SVM12) to 5%  $O_2$  + 20%  $H_2O$  +  $N_2$  (Bal) + KCl(s)/KCl(g) for 168 hours at 600°C. The impact of sample position could be evaluated, and many samples could be set up simultaneously, which is a key factor in running very long exposures in an effective way. Mass gain measurements revealed that all the reference material samples exhibited mass gains in the range of 4.7–6.8 mg/cm<sup>2</sup>, with average mass gain of 6.1 mg/cm<sup>2</sup> and a spread of  $\pm 0.7$  mg/cm<sup>2</sup> (Figure 7.2). This shows that all the samples experienced a similar corrosion attack, regardless of the sample position. The spread in mass gain data can be attributed in part to the occurrence of oxide spallation as the samples cooled down after exposure, although it might also be interpreted as a natural variation among the samples. It is well-known that there will be a variation in mass gain with parallel samples that have pre-deposited KCl(s) [89], and the variation observed among the high number of samples in the present set-up is considered to be within the expected range. The set-up also forms the foundation for long exposures where small deviations between replicate samples will play a very limited role. The samples that experienced spallation, marked with asterisks in Figure 7.2, were not considered when calculating the average mass gain. The corrosiveness of the test conditions, i.e., KCl and water vapour at 600°C, was evident from the high mass gains of the samples, which indicated that breakaway oxidation had been induced and that the alloy had transitioned into the secondary protection regime. High mass gain is associated with rapid oxidation kinetics and rapid oxide growth rates, as reported previously [57,66].

The robustness testing was important for conducting the long-term corrosion investigation, in which several materials and coatings would be exposed at the same time under the same conditions.

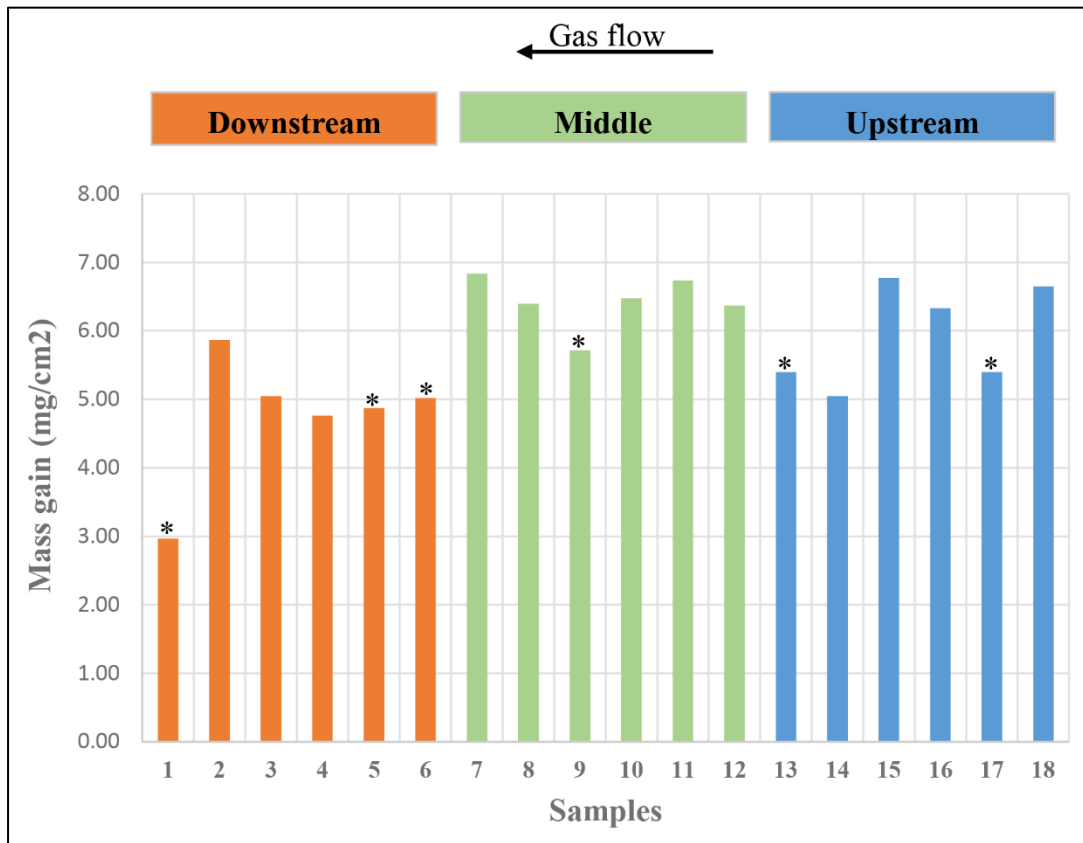


Figure 7.2: Mass gains for 18 samples of reference material SVM12 after exposure to 5% O<sub>2</sub> + 20% H<sub>2</sub>O + N<sub>2</sub> (Bal) + KCl(s)/KCl(g) for 168 hours at 600°C. The asterisks (\*) indicate samples that experienced spallation.

## 7.2 Long-term corrosion behaviours of bulk materials and coatings

### 7.2.1 Corrosion resistance

To investigate the corrosion resistance mechanisms of the different materials/coatings, both bulk and overlay weld coatings were exposed to 5% O<sub>2</sub> + 20% H<sub>2</sub>O + N<sub>2</sub> (Bal) + KCl(s)/KCl(g) for 500 hours. Prior to these exposures, 0.5 mg/cm<sup>2</sup> KCl was sprayed onto the samples. In this first round of long-duration exposures, the materials were selected to include both bulk materials and coatings of similar composition and the results of this investigation was basis for paper I [74]. Corrosion resistance was evaluated based on the average oxide thickness, as measured from the SEM-BSE images. Several thickness measurements were obtained from representative regions that showed no signs of spallation, and the average value was calculated and is presented in Figure 7.3. The variation in thickness across the region is presented as a range. Oxide thickness was considered for this task because it depicts the actual extent of corrosion attack, in contrast to mass gain measurements, which reflect the general corrosion behaviour of the material.

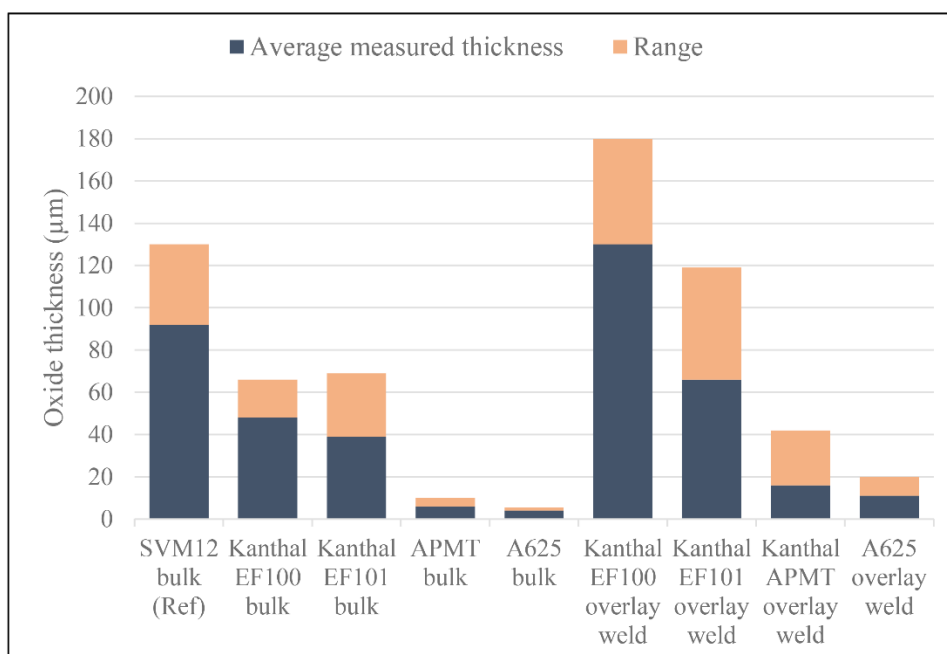


Figure 7.3: Oxide thicknesses of the bulk materials and overlay weld coatings after exposure for 500 hours to 5% O<sub>2</sub> + 20% H<sub>2</sub>O + N<sub>2</sub> (Bal) + KCl(s)/KCl(g) at 600°C. The samples were sprayed with 0.5 mg/cm<sup>2</sup> KCl prior to exposure.

All the bulk materials and coatings experienced breakaway oxidation, which resulted in thick oxide scales after 500 hours, as compared to what would be expected in the primary regime (Cr<sub>2</sub>O<sub>3</sub>/Al<sub>2</sub>O<sub>3</sub> scales). In general, the overlay weld coatings formed thicker oxide scales than the bulk materials of similar composition. Among the bulk materials, the reference material (SVM12) formed the fastest-growing/thickest scale (about 120–130 μm), followed by the ferritic steels (Kanthal<sup>®</sup> EF100, Kanthal<sup>®</sup> EF101 and APMT), and A625 formed the thinnest scale (about 5.5 μm). A similar trend was observed for the overlay weld coatings. The oxide thickness measurements clearly showed the variation in corrosion resistance among the tested alloys. This variation may be due to the different incubation times to breakaway oxidation, or the types of oxides formed after breakaway oxidation by the respective alloys, which in turn are influenced by the alloy composition. In general, the formation of such thick oxide scales in an aggressive environment is an indication of a short incubation time to breakaway oxidation, which leads to faster oxide transformation into the secondary corrosion regime.

SEM/EDS analysis of ion-milled cross-sections of the reference material (SVM12) showed that this alloy formed a thick and dense two-layered oxide scale that could be divided into an outward-growing layer and inward-growing layer (Figure 7.4). Both oxide layers contained cracks, which might have been induced during sample preparation after exposure. The outward-growing layer was composed of Fe-oxide, while the inward-growing layer was a mixed spinel, indicating diffusion-controlled kinetics in combination with an electrochemical mechanism, whereby growth of the scale is governed by the diffusivity of different cations through the scale.

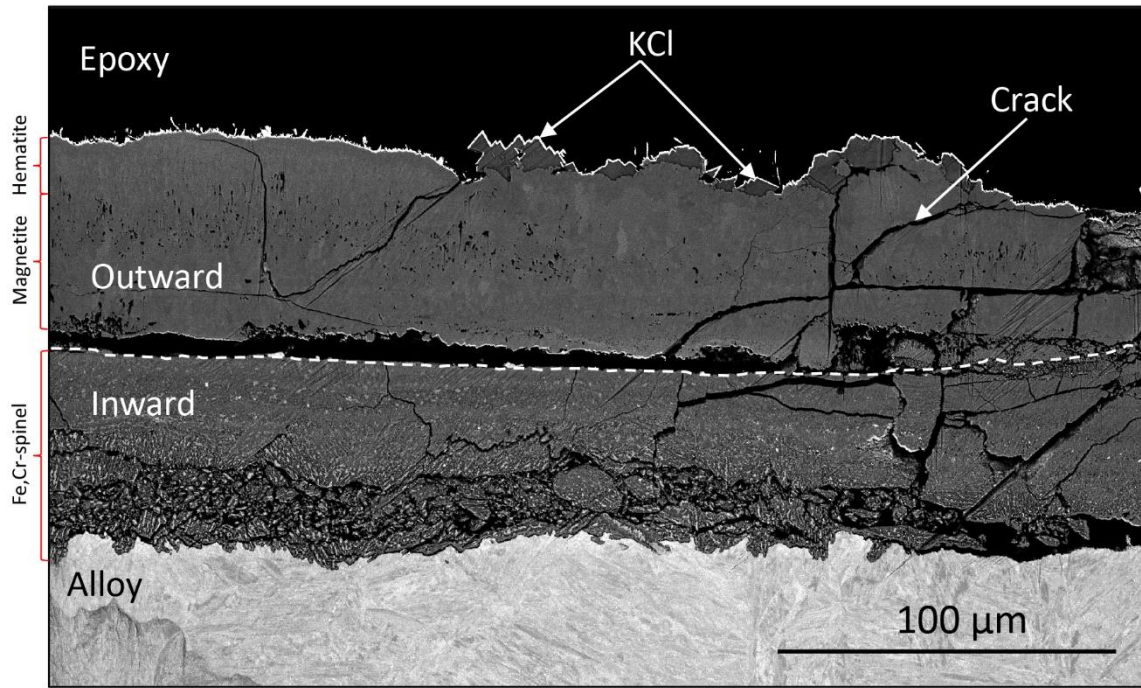


Figure 7.4: SEM-BSE cross-sectional image of SVM12 after exposure to 5% O<sub>2</sub> + 20% H<sub>2</sub>O + N<sub>2</sub> (Bal) + KCl(s)/KCl(g) for 500 hours at 600°C.

The microstructural investigations of all the samples, besides SVM12, showed that all the alloys formed double-layered scales (Figure 7.5). The outward-growing layers of all the ferritic steels consisted of Fe-rich oxide, while the inward-growing layers were identified as Fe,Cr,Al,Si-oxide. This is as expected given the different mobilities of the different cations through the scale. The elemental distribution in the inward-growing layers varied for the ferritic steels, and this may explain the observed variation in corrosion resistance among these alloys. The effects of alloying elements such as Cr and Al on the secondary protection of alloys have previously been reported [57,90,91]. In the current study, it is clear that a chromium-/aluminium-rich inner scale improves corrosion resistance. The order of corrosion performance is closely associated with the chromium content of the inner scale of each alloy. In the case of the ferritic steels, the order of performance is: Kanthal® EF100 < Kanthal® EF101 < APMT (weakest to strongest performance in terms of corrosion resistance).

The bulk Ni-based alloy A625 exhibited the best corrosion resistance, as indicated by the thin oxide scale of about 5.5 μm (Figure 7.5 d<sub>1</sub>). The scale was double-layered and could be divided into outward- and inward-growing layers, with K<sub>2</sub>CrO<sub>4</sub> particles present at the surface. This indicates that oxide growth results from a reaction between the chromium-rich oxide and KCl, according to Eq. (4.7) in Section 4.2.2. The outward-growing scale consisted of a Ni-rich oxide and the inward-growing scale consisted of a Cr-rich oxide. Below the scale, A625 formed a 4-μm-thick fine-grain region (FGR).

The improved secondary protection exhibited by A625 is attributed to chromium enrichment in the inner scale, which may act as a barrier and prevent ions from diffusing through and, thereby, mitigating further corrosion. In addition, it is possible that the formed FGR contributes with fast diffusion paths for chromium from the alloy substrate, which leads to chromium enrichment in the inner scale. This is supported by the fact that the FGRs are depleted of chromium and enriched in nickel. The results from this study indicate that the secondary

protection is dependent upon the microstructure of the inward-growing scale, the alloy composition, and the diffusivity of cations, and is not dependent upon the corrosive elements, such as K and Cl.

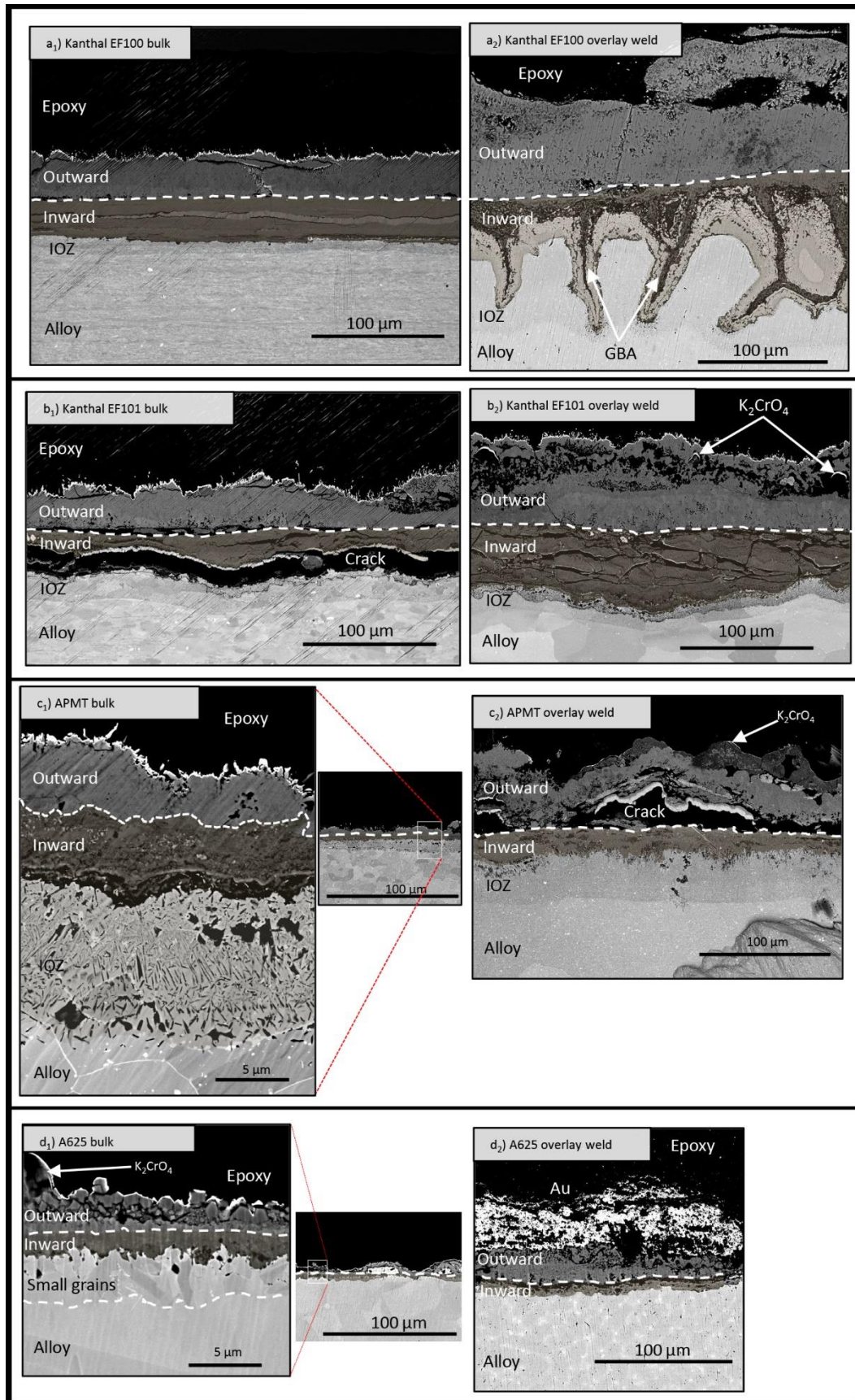


Figure 7.5: SEM-BSE cross-sectional images of the bulk materials and overlay weld coatings after exposure to 5% O<sub>2</sub> + 20% H<sub>2</sub>O + N<sub>2</sub> (Bal) + KCl(s)/KCl(g) for 500 hours at 600°C. The samples were sprayed with 0.5 mg/cm<sup>2</sup> KCl prior to exposure.

| Bulk materials | Outward-growing scale |       |    |          | Inward-growing scale |    |    |            |
|----------------|-----------------------|-------|----|----------|----------------------|----|----|------------|
|                | Fe                    | Cr    | Al | Others   | Fe                   | Cr | Al | Others     |
| SVM12          | 100                   | -     | -  |          | 60                   | 35 | -  | -          |
| Kanthal EF100  | 100                   | -     | -  |          | 55                   | 25 | 20 |            |
| Kanthal EF101  | 100                   | -     | -  |          | 35                   | 40 | 20 |            |
| APMT           | 100                   | -     | -  |          | 15                   | 60 | 20 | Si=2; Mo=3 |
| A625           | 5-20                  | 20-35 | -  | Ni=40-70 | 3                    | 70 | -  | Ni=25      |

Figure 7.6: Elemental distributions in the outward-growing and inward-growing layers of the scales formed by the bulk materials after exposure to 5% O<sub>2</sub> + 20% H<sub>2</sub>O + N<sub>2</sub> (Bal) + KCl(s)/KCl(g) for 500 hours at 600°C.

As previously mentioned, all of the overlay weld coatings exhibited thicker oxide scales than the bulk materials of similar composition. The SEM/EDS analysis revealed that the inward-growing scales of the overlay weld coatings contained less chromium than was the case for the bulk materials (compare Figure 7.6 and Figure 7.7).

| Overlay weld coatings | Outward-growing scale |    |    |        | Inward-growing scale |    |    |             |
|-----------------------|-----------------------|----|----|--------|----------------------|----|----|-------------|
|                       | Fe                    | Cr | Al | Others | Fe                   | Cr | Al | Others      |
| Kanthal EF100         | 100                   | -  | -  | -      | 35                   | 35 | 30 | -           |
| Kanthal EF101         | 100                   | -  | -  | -      | 50                   | 30 | 15 | Si=5        |
| APMT                  | 100                   | -  | -  | -      | 5                    | 50 | 20 | Si=2        |
| A625                  | 15                    | 5  | -  | Ni=80  | 10                   | 30 | -  | Ni=55; Mo=5 |

Figure 7.7: Elemental distributions in the outward-growing and inward-growing layers of the scales formed by the overlay weld coatings after exposure to 5% O<sub>2</sub> + 20% H<sub>2</sub>O + N<sub>2</sub> (Bal) + KCl(s)/KCl(g) for 500 hours at 600°C.

### 7.2.2 Why bulk materials perform better than overlay weld coatings

To investigate further why the bulk materials exhibited better corrosion resistance than the overlay weld coatings of similar composition, a detailed microstructural investigation was performed on Kanthal<sup>®</sup> EF101 bulk material overlay weld coating at 600°C with 0.5 mg/cm<sup>2</sup>

pre-deposited KCl, using SEM/EDS of ion-milled cross-sections and STEM/EDS of the FIB lamella.

SEM/EDS analysis of the unexposed bulk and overlay weld coating of Kanthal® EF101 revealed differences in the alloy microstructures. The alloy grain sizes differed between the two cases and were in the ranges of 11–40  $\mu\text{m}$  (bulk) and 20–70  $\mu\text{m}$  (overlay weld coating). This was the result of different manufacturing processes. The bright particles within the alloy grains and along the grain boundaries were identified as precipitates of reactive elements (REs). The bulk material consisted of larger RE precipitates (about 1–3  $\mu\text{m}$ ) than those in the overlay weld coating (about 1  $\mu\text{m}$ ). Although the effect of REs on corrosion protection is not investigated in this thesis, it is worth mentioning that studies have shown that the addition of REs improves corrosion resistance by promoting the inward scale growth and adhesion [92–95].

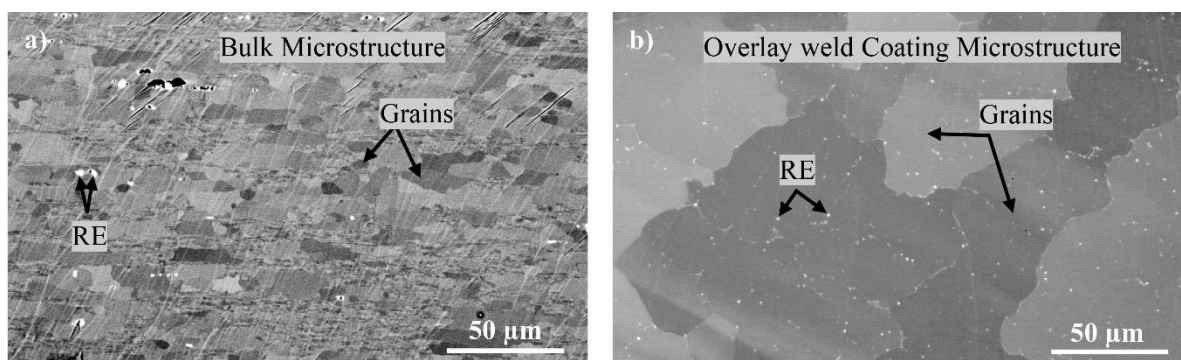


Figure 7.8: SEM-BSE images of ion-milled EF101 before exposure: a) bulk material; b) overlay weld coating.

Since the main difference in elemental distribution was observed for the inward-growing scales, which could be the reason for the observed variation in oxide resistance in the secondary regime between the Kanthal® EF101 bulk material and the Kanthal® EF101 overlay weld coating, a detailed microstructural investigation was conducted on the complex inward-growing scales. Figure 7.9 shows the locations of the TEM lift-outs.

The STEM/EDS analysis of the Kanthal® EF101 bulk sample revealed that this alloy formed an oxide scale that consisted of outward-growing and inward-growing scales (in accordance with the findings from the SEM/EDS analysis) (Figure 7.10). In the inner regions of the inward-growing scale, the bulk material formed a **1.0–1.2- $\mu\text{m}$ -thick chromium-rich** oxide (59–65 at% Cr, 26–30 at% Fe, 3–10 at% Al, and 1–2 at% Si), which was accompanied by a **2- $\mu\text{m}$ -deep chromium-depleted zone** beneath the scale. Such high concentrations of trivalent ions (Cr and Al) in the inner scale would result in a total >67.7 cationic%, which represents the maximum concentrations of divalent and trivalent ions in a spinel structure [96]. Therefore, it is proposed that the oxide transforms into a corundum type of oxide, which is more-protective.

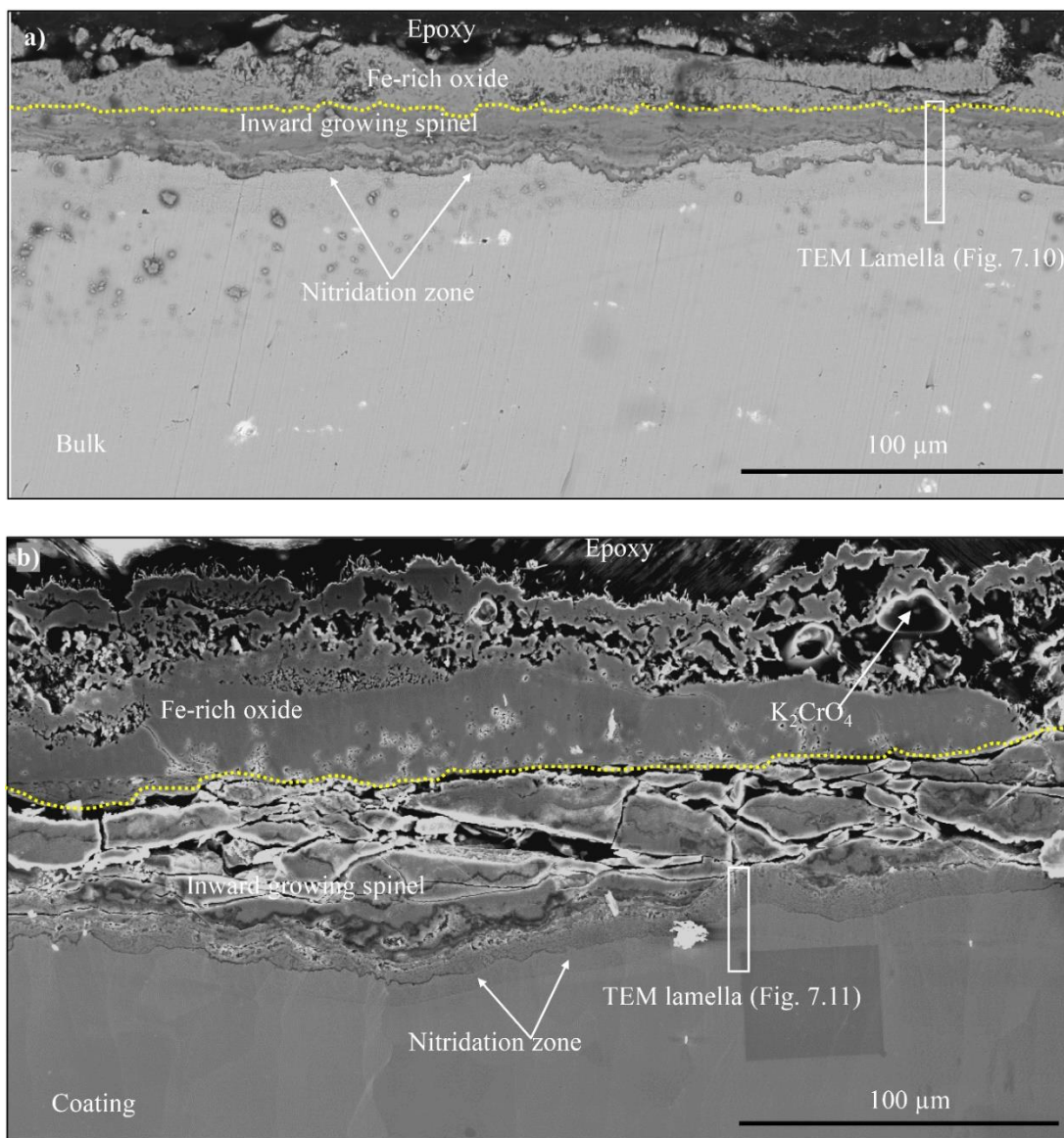


Figure 7.9: SEM-BSE cross-sectional images of Kanthal® EF101 exposed to 5% O<sub>2</sub> + 20% H<sub>2</sub>O + N<sub>2</sub> (Bal) + KCl(s)/KCl(g) for 500 hours at 600°C. The black rectangles indicate the regions of TEM lift-out for: a) the bulk material; and b) the overlay weld coating.

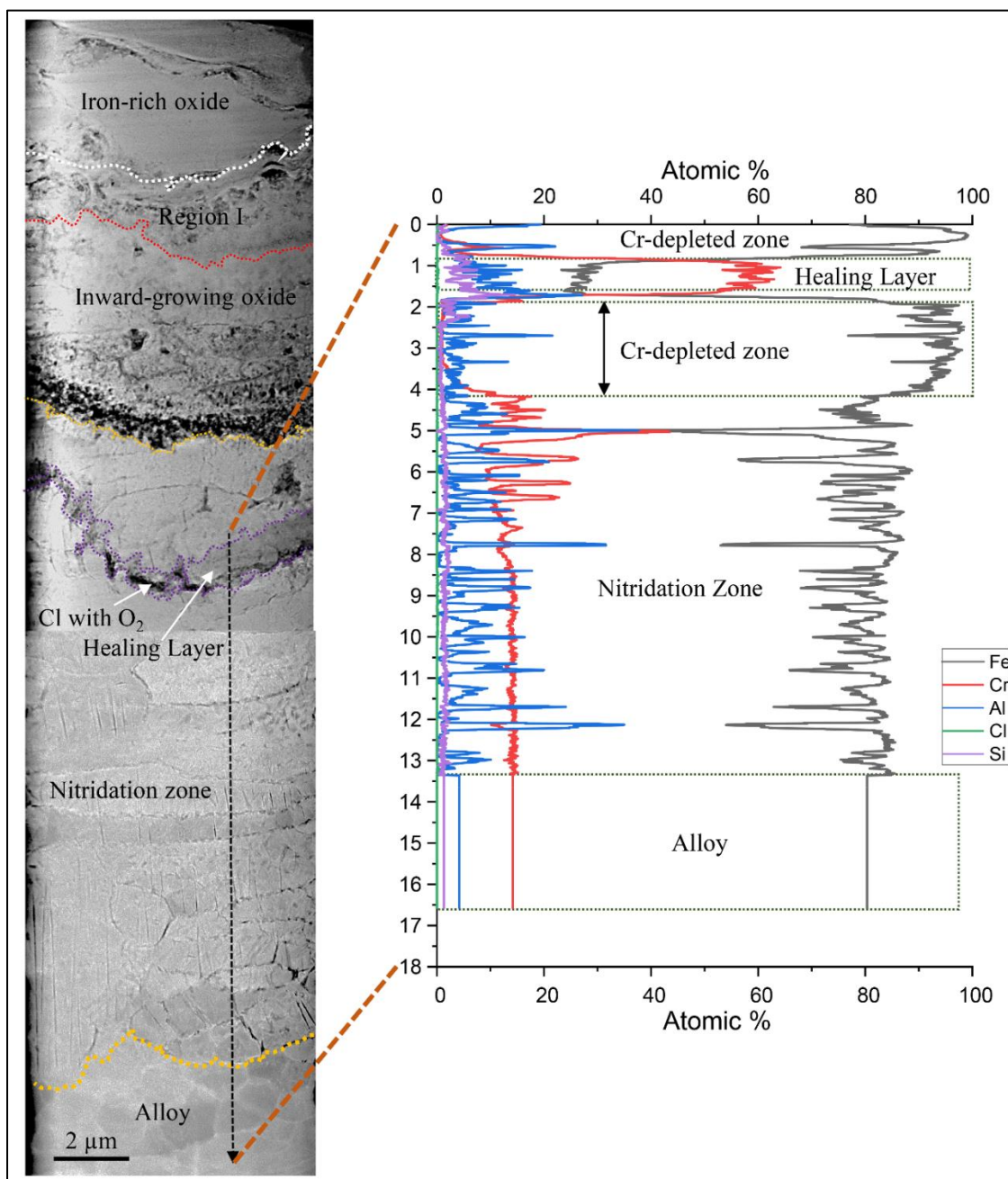


Figure 7.10: HAADF-STEM image of bulk Kanthal® EF101 lamella, and STEM/EDS line-scan of the elemental distribution in the lower regions of the inward-growing scale.

The overlay weld coating formed a **thinner chromium-rich oxide layer (300–500 nm)** close to the metal-scale interface, with composition of 60–65 at% Cr, 30–40 at% Fe, 3–5 at% Al, and 2–5 at% Si, which was accompanied by a **1-μm-deep chromium-depletion zone**. This chromium-rich oxide consisted of mixed spinel and a corundum type of oxide. The results of the oxide microstructural investigation indicate that the superior corrosion resistance displayed by the bulk material, as compared to the overlay weld coating, is partly due to more-rapid formation of a protective chromium-/aluminium-rich layer beneath the inward spinel scale (the I region in Figure 7.10). This may be explained by the smaller grains in the bulk alloy compared to the overlay welded material (Figure 7.8). The oxidation process of the bulk material is transformed more rapidly into better secondary protection by the formation of a healing layer,

which consists of a chromium-rich corundum type of oxide at the metal/oxide interface. This has earlier been shown to depend on the diffusivity and activity of Cr/Al [57].

Another corrosion feature observed for both the bulk material and the overlay weld coating was the formation of nitridation zones (NZ) beneath the scales with aluminium nitrides (AlN). The occurrence of NZ implies that the formed scales are permeable to  $N_2$  due to defects in the oxides. In this study, the depth of the formed NZ was in the same range in both cases, i.e., 12–16  $\mu\text{m}$  (bulk material) and 10–17  $\mu\text{m}$  (overlay weld coating). However, the size of the AlN particles differed, i.e., about 300–650 nm for the bulk material and 150–550 nm for the overlay weld coating, indicating faster diffusion of  $N_2$  for the bulk material. Although the effects of AlN formation on the corrosion properties of the alloys were not investigated in this study, it seems plausible that the corrosion property becomes impaired because this process sequesters aluminium in the form of AlN, which would otherwise have contributed to formation of a more-protective scale. From the mechanical property perspective, alloy nitridation has been reported to reduce the ductility and induce the embrittlement of the alloy [97].

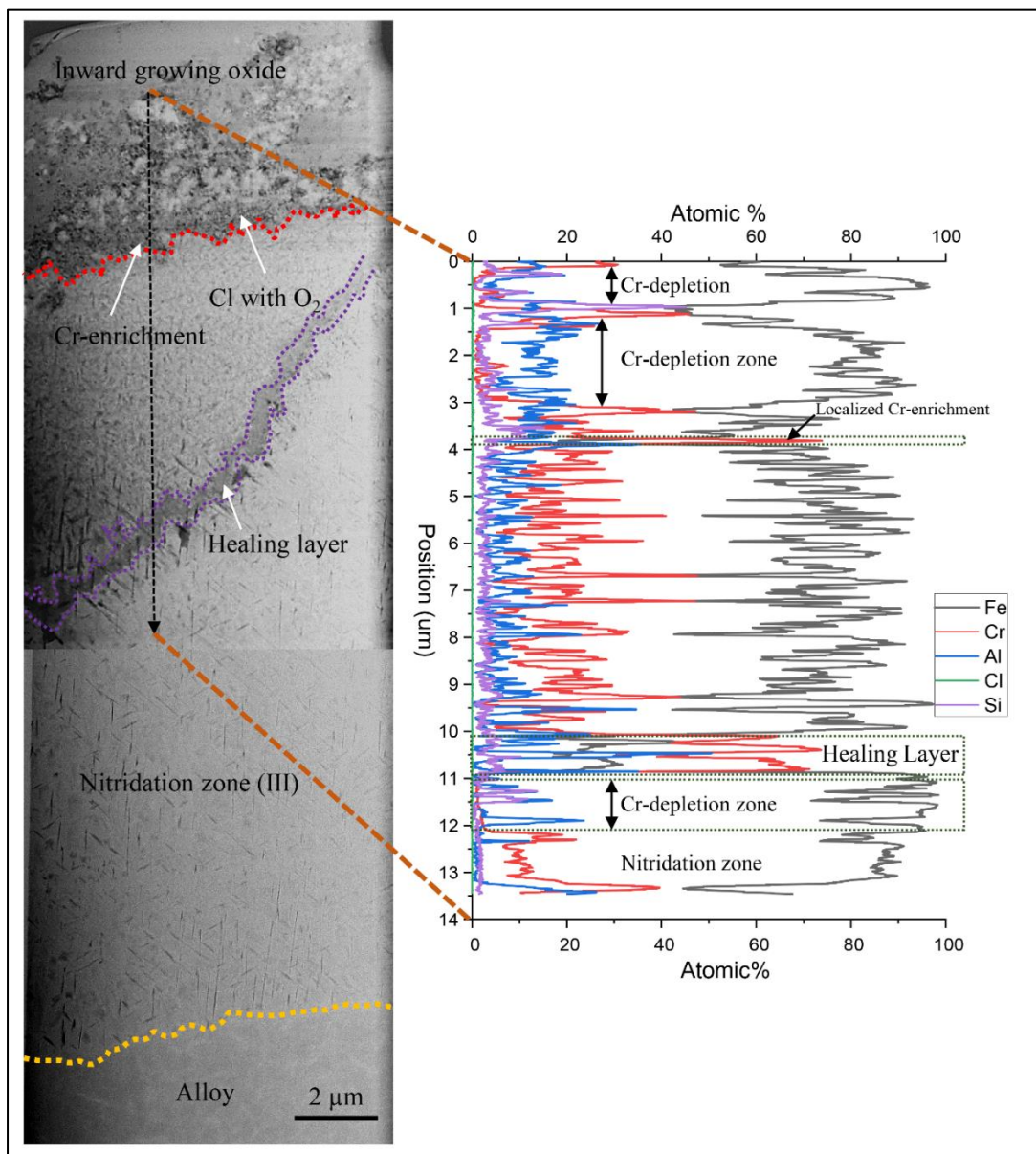


Figure 7.11: HAADF-STEM image of the overlay weld Kanthal® EF101 lamella, and STEM/EDS line-scan of the elemental distribution in the inward-growing scale.

### 7.2.3 Microstructural evolution after breakaway oxidation

The life-times of alloys used in boiler applications are dictated by their long-term corrosion behaviours. Understanding the microstructural evolution of the oxide scales formed by a high-temperature alloy makes it possible to predict its life-time. In this thesis, the microstructural evolution of the oxide scales formed by SVM12, APMT and Alloy 27Cr33Ni3Mo after exposure to 5% O<sub>2</sub> + 20% H<sub>2</sub>O + N<sub>2</sub> (Bal) + KCl(s)/KCl(g) for 168 hours, 1,000 hours, and 8,000 hours, were investigated. The selected alloys represent different material classes that are suitable for applications in harsh boiler environments. For these exposures, 2 mg/cm<sup>2</sup> KCl was pre-deposited on the sample surfaces to induce breakaway oxidation and to ensure that KCl(s) was present on the surface throughout the exposure. Characterisation of corrosion products was performed using SEM/EDS, SEM/EBSD on ion-milled cross-sections, and XRD. In addition, thermodynamic modelling of stable oxide phases and kinetic simulations were performed for comparisons with the experimental results. For the purpose of interpretation of the data and comparison with the experimental results in the complex and corrosive environment, the thermodynamic calculations were focused on the inward-growing scale.

The oxidation kinetics results are based on the average oxide thicknesses calculated from several measurements made in representative regions of SEM-BSE images of the ion-milled cross-sections. The error bars represent the variation in thickness across the regions. As shown in Figure 7.12, all the tested alloys experienced breakaway oxidation and transitioned into the secondary corrosion regime already after 168 hours of exposure. The 12 wt% Cr SVM12 alloy exhibited the fastest oxidation kinetics, forming thick oxide scales, i.e., 91 µm after 168 hours to about 206 µm after 8,000 hours of exposure. The rapid scale growth exhibited by this alloy is attributed to a limited supply of chromium from the alloy to the corrosion front to form/reform a protective scale. Similar oxidation kinetics have been reported for pure iron [65] and low-iron steels [57] after breakaway oxidation, with the exception of forming FeO. Further investigations of the oxidation kinetics of SVM12 showed that the order of parabolicity according to the parabolic law  $x^{\alpha} \propto t$  ( $\alpha$ -value) was  $>2$ , suggesting a sub-parabolic growth relationship that results from oxide grain growth.

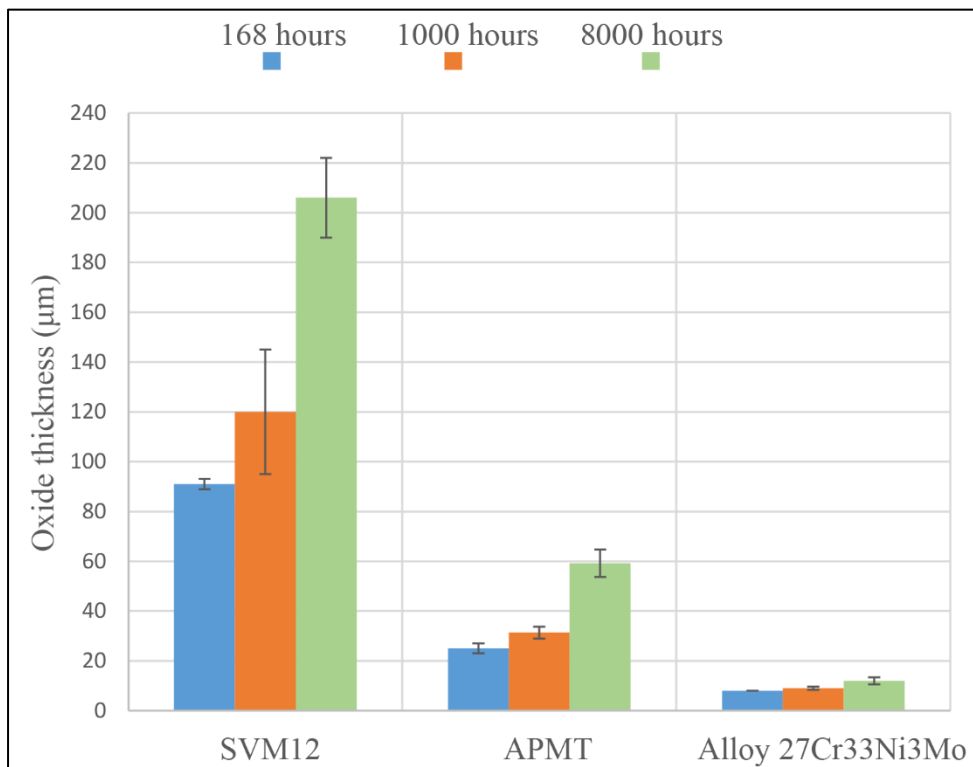


Figure 7.12: Average oxide thicknesses of the tested alloys after exposure to 5% O<sub>2</sub> + 20% H<sub>2</sub>O + N<sub>2</sub> (Bal) + KCl(s)/KCl(g) for 168 hours, 1,000 hours and 8,000 hours at 600°C.

In contrast, the high-alloy steels (APMT and Alloy 27Cr33Ni3Mo) exhibited lower oxide growth rates and formed thinner oxide scales after breakaway. The formation of slow-growing scales indicates good secondary protection, and may be attributed to the formation of Cr/Al-rich, inward-growing scales, which may retard the oxidation process.

Microstructural investigations showed that all the alloys form double-layered scales, i.e., outward-growing and inward-growing scales after breakaway oxidation, during all the exposures. The results of the investigation are presented and discussed further for each alloy in the next sections.

### Martensitic stainless steel – SVM12 (12 wt% Cr)

An analysis based on the results obtained using SEM/EDS, SEM/EBSD and XRD showed that the scales formed by SVM12 consisted of outward-growing layers (region I) and inward-growing layers (region II), as shown in Figure 7.13. Potassium chromate formation was observed at the top of the scale and, in some cases, embedded in the outward-growing scale. The outer scale was composed of Fe-rich oxides, identified as hematite and magnetite, and the inner layers were composed of FeCr-spinel, in all the exposures. This pattern of elemental distribution and oxide phase arrangement can be explained by the different diffusivities of cations through the spinel [67], with Fe exhibiting faster diffusion rates than Cr. Furthermore, the elemental analysis showed that the lower regions of the inner scale (region III) became enriched in chromium over time (from 40 at% after 168 hours to 65 at% after 8,000 hours).

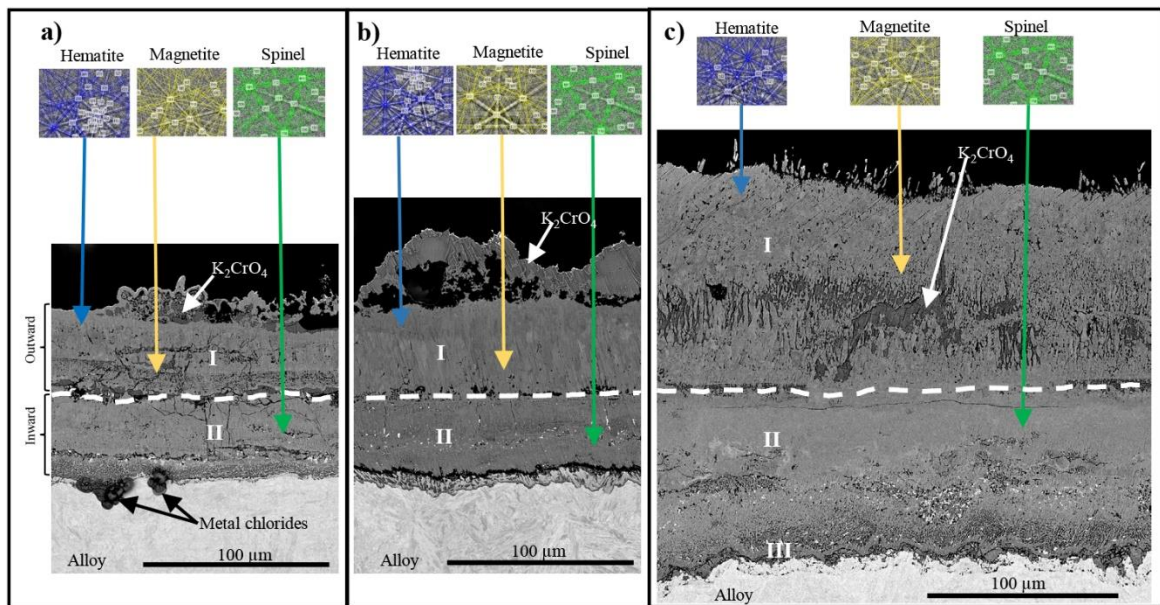


Figure 7.13: SEM-BSE cross-sectional images of SVM12, showing the evolution of the oxide microstructure after exposure to 5% O<sub>2</sub> + 20% H<sub>2</sub>O + N<sub>2</sub> (Bal) + KCl(s)/KCl(g) for: a) 168 hours; b) 1,000 hours; and c) 8,000 hours at 600°C.

The experimental observations are in good agreement with the results of the thermodynamic calculations, which predict spinel as the major phase of the inward-growing scale (see Figure 7.14). Moreover, the calculations predict the formation of a minor fraction of the corundum type of oxide ( $\sim 22\%$ ) at low oxygen partial pressures ( $<10^{-30}$ ) closer to the metal/scale interface. However, identification of the crystalline phase from the experimental investigations revealed the absence of corundum-type structures in these regions. Despite chromium enrichment of the inner scale over time, this alloy retained the spinel structure even after a very long exposure. Instead, scale growth was manifested as a rapid diffusion-controlled process owing to the outward flux of Fe via the grain boundaries of the spinel (magnetite), leading to poor secondary protection. It is plausible that this alloy might form the corundum type of oxide in the inner scale, as predicted by the thermodynamic calculations, after even longer exposure time. However, due to the fast scale growth, the oxide scale might become too-thick and experience spallation, in which case the integrity of the oxide scale would be lost.

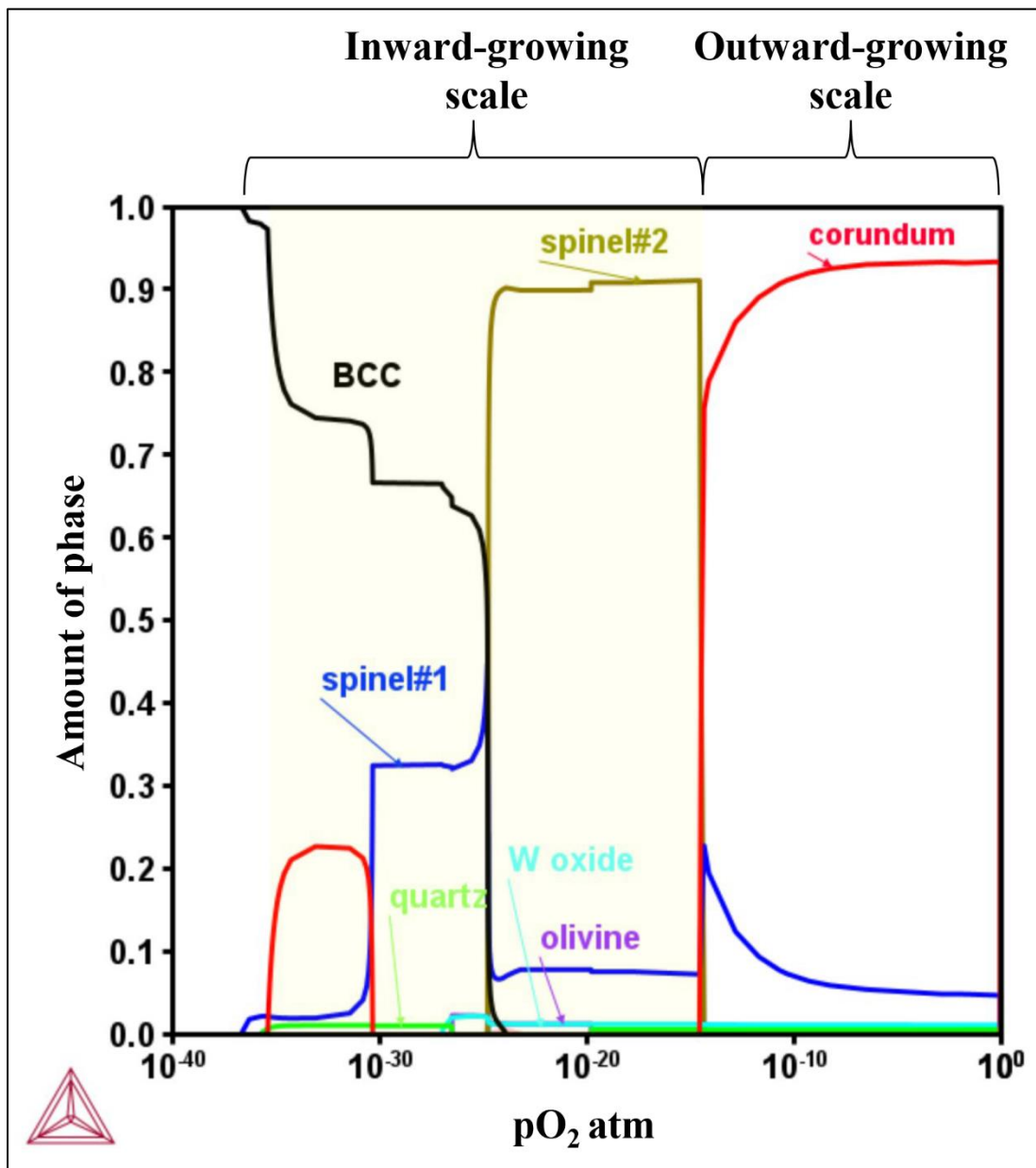


Figure 7.14: Equilibrium calculations showing the amount of predicted stable phases plotted against  $pO_2$  for SVM12.

### FeCrAl - APMT

The oxide microstructural investigation showed that the FeCrAl alloy (APMT) exhibited a slow oxidation rate and formed thin oxide scales (thicknesses of 25  $\mu\text{m}$ , 31  $\mu\text{m}$ , and 59  $\mu\text{m}$  after 168 hours, 1,000 hours, and 8,000 hours, respectively), as shown in Figure 7.15 a, b, and c. The scales were characterised by the formation of potassium chromate on the surface in all the exposures. Similar to SVM12, the scales formed by APMT were double-layered, consisting of outward-growing and inward-growing layers. The SEM/EDS and SEM/EBSD analyses revealed that the outward-growing scales consisted of iron-rich oxides, identified as hematite on top of magnetite, and that the inward-growing scales consisted of spinel. The SEM/EDS elemental analysis showed that the inner scale became enriched in chromium over time, followed by the appearance of chromium-depletion zones (to depths of 12  $\mu\text{m}$  and 20  $\mu\text{m}$  after 1,000 and 8,000 hours of exposure, respectively). Chromium enrichment of the inner scale

resulted in phase transformation from a spinel oxide to a corundum type of oxide. These microstructural changes in the oxide are attributed to the high levels of alloying elements (chromium and aluminium) in the spinel and in the alloy (21-wt% Cr). It has been shown in previous studies that increasing the chromium and aluminium contents of the alloy contributes to improvement of the corrosion resistance of the alloy [57,96,98]. It should be noted that small amounts of K and Cl were observed in the inner scale. However, these elements exerted no influence on the formation of good secondary protection after breakaway oxidation. Instead, the scale growth for this alloy followed a diffusion-controlled mechanism and displayed a slower sub-parabolic growth relationship in the secondary corrosion regime.

Furthermore, APMT formed NZ beneath the scales, which deepened over time, i.e., from a depth of 28  $\mu\text{m}$  after 1,000 hours to 74  $\mu\text{m}$  after 8,000 hours of exposure. However, the NZ was not observed after 168 hours. The process of formation of NZ has been reported to be retarded due to the slow progress of the processes of  $\text{N}_2$  dissociation, dissolution, and nitride nucleation [99]. It is possible that after 168 hours, nitridation had simply not occurred yet. This might explain the observed growth of the NZ from 1,000 hours to 8,000 hours. As mentioned in Section 7.2.2, the formation of NZ might have negative consequence for both the corrosion and mechanical properties of the alloy.

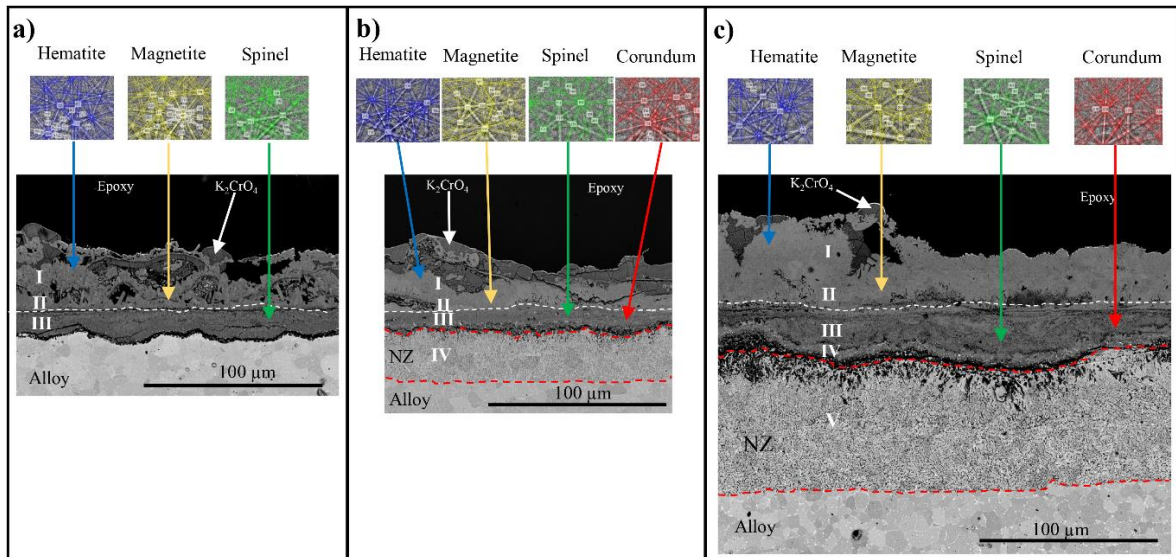


Figure 7.15: SEM-BSE cross-sectional images of APMT, showing the evolution of the oxide microstructure after exposure to 5%  $\text{O}_2$  + 20%  $\text{H}_2\text{O}$  +  $\text{N}_2$  (Bal) +  $\text{KCl(s)}/\text{KCl(g)}$  for: a) 168 hours; b) 1,000 hours; and c) 8,000 hours at 600°C.

The experimental findings for the long-term oxidation behaviour of APMT agree well with the thermodynamic calculations, which predict the formation of spinel and a larger fraction of the corundum phase in the lower oxygen partial pressure regions (inward-growing scale) (Figure 7.16).

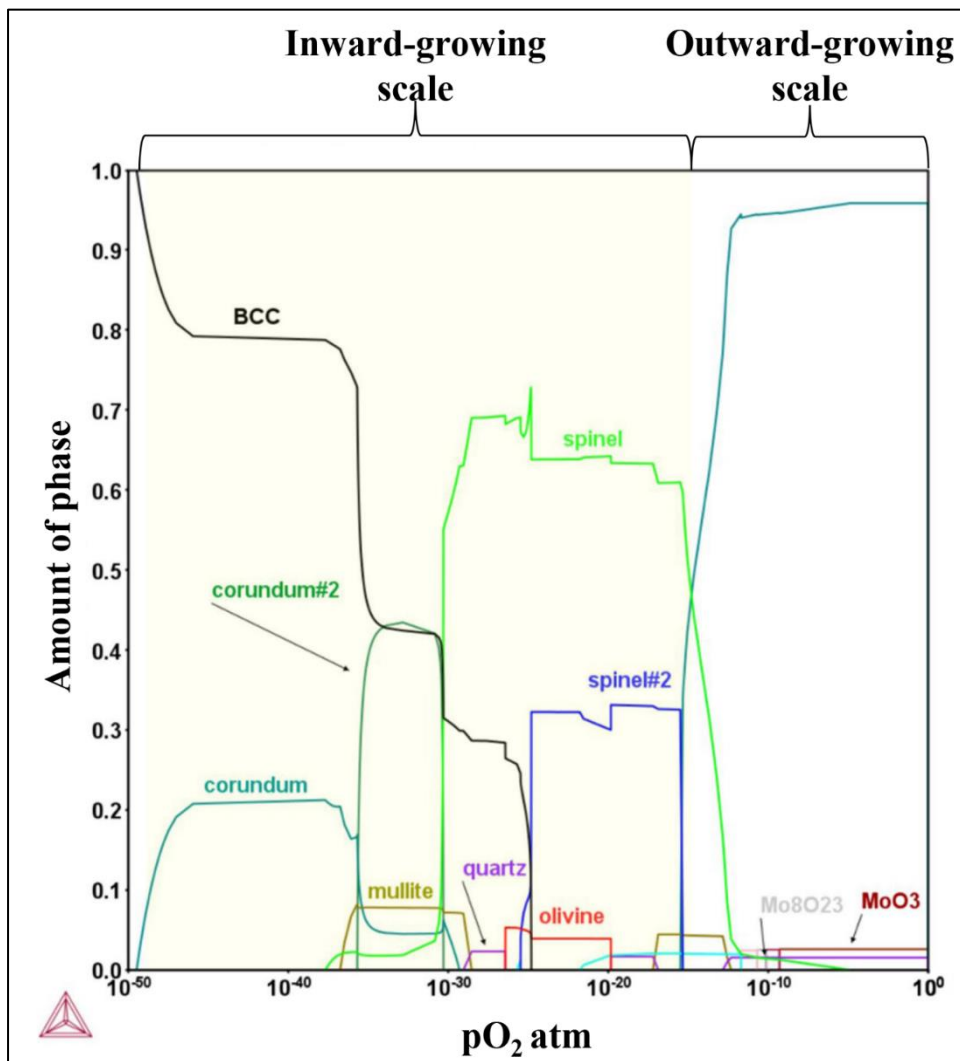


Figure 7.16: Equilibrium calculations showing the amount of predicted stable phases plotted against  $pO_2$  for APMT.

#### Austenitic stainless steel - Alloy 27Cr33Ni3Mo

Alloy 27Cr33Ni3Mo exhibited the slowest oxidation kinetics and formed the thinnest oxide scales, as compared with SVM12 and APMT. The SEM/EDS and SEM/EBSD analyses showed that the formed scales were double-layered, consisting of outward-growing and inward-growing scales (Figure 7.17). The scale growth was diffusion-controlled and exhibited a slow sub-parabolic growth relationship. Initially (after a 168-hour exposure), the scale consisted of iron-rich spinel in the outer layer and chromium-rich spinel in the inner layer. As the oxidation progressed, the outer scales became enriched in Fe, while the inner scale became enriched in chromium. The SEM/EDS elemental distribution analysis showed that the inward-growing scale was composed of 80 at% Cr and 90 at% Cr after 1,000 hours and 8,000 hours, respectively. The enrichment of chromium led to phase transformation from spinel to corundum at 1,000 and 8,000 hours. The formation of a protective corundum type of oxide within the secondary corrosion regime contributes to improved corrosion resistance. This may explain the slow oxidation kinetics exhibited by this alloy even after long-term exposure.

Furthermore, it was observed that Alloy 27Cr33Ni3Mo formed FGRs close to the metal/scale interface, which were chromium-depleted and nickel-enriched. As oxidation progressed, the

FGRs increased in depth, from 4  $\mu\text{m}$  after 168 hours to 19  $\mu\text{m}$  after 8,000 hours. Alloy grain refinement leads to an increased number of grain boundaries, which increases the grain boundary diffusion of ions. Studies of the effects of alloy grain size on the corrosion behaviours of alloys have shown that finer grains lead to improved corrosion behaviours [100,101]. The results of this study agree with the findings of the aforementioned studies.

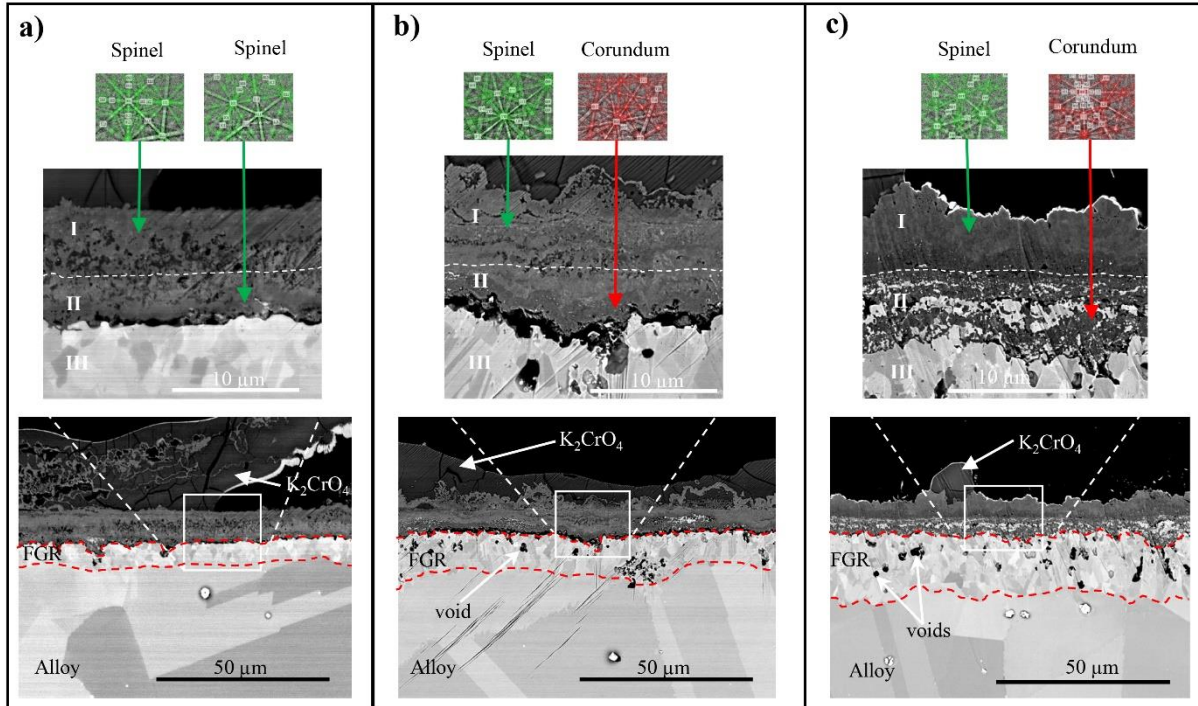


Figure 7.17: SEM-BSE cross-sectional images of Alloy 27Cr33Ni3Mo, showing the evolution of the oxide microstructure after exposure to 5%  $\text{O}_2$  + 20%  $\text{H}_2\text{O}$  +  $\text{N}_2$  (Bal) +  $\text{KCl(s)}/\text{KCl(g)}$  for: a) 168 hours; b) 1,000 hours; and c) 8,000 hours at 600°C.

From the thermodynamic modelling perspective, the calculated oxide phases (in Figure 7.18) agree well with the identified crystalline phases in the experimental investigations.

Further investigations of the growth kinetics of the corundum phase formed by Alloy 27Cr33Ni3Mo showed that the experimental kinetics were faster than the DICTRA-simulated kinetics, as shown in Figure 7.19. The measured thickness of the corundum phase increased from  $\sim 1.4 \mu\text{m}$  after 1,000 hours to  $\sim 5.3 \mu\text{m}$  after 8,000 hours, indicating that the fraction of corundum in the inner scale increases as oxidation progresses due to phase transformation from the spinel oxide. Similar phase transformation has been reported in another study conducted under the same experimental conditions [102]. It is concluded that the good secondary protection exhibited by Alloy 27Cr33Ni3Mo is due to the formation of corundum type of oxide through phase transformation from Cr-rich spinel oxide, as facilitated by a continuous supply of chromium via the increased number of grain boundaries in the FGRs.

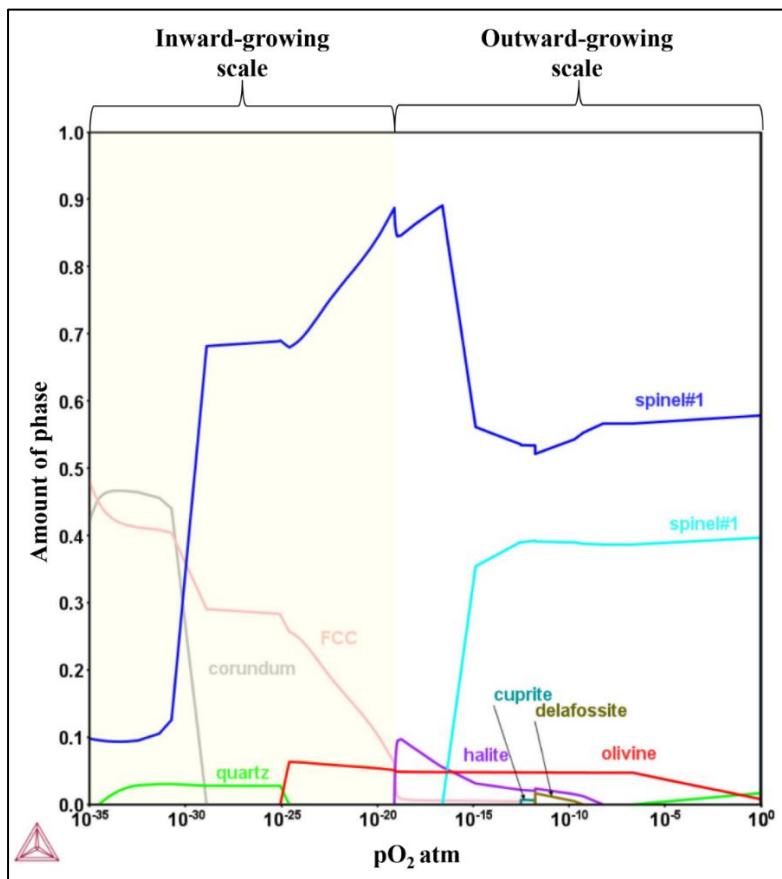


Figure 7.18: Equilibrium calculations showing the amount of predicted stable phases plotted against  $pO_2$  for Alloy 27Cr33Ni3Mo.

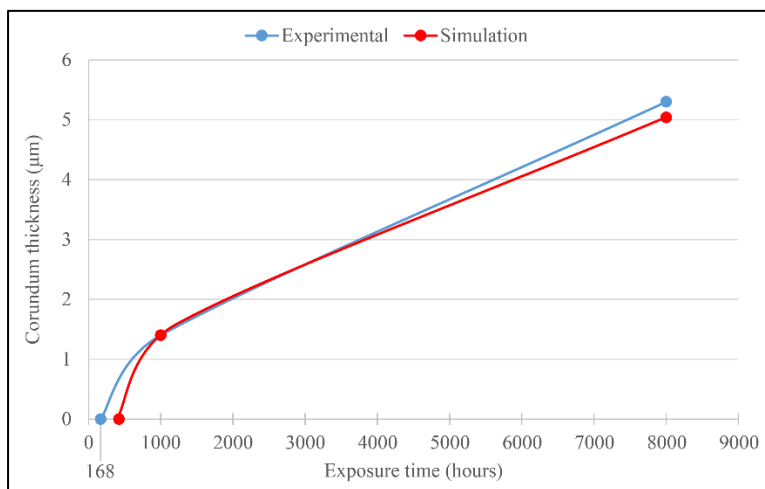


Figure 7.19: Growth kinetics of the Cr-rich corundum oxide in the inward-growing scale of Alloy 27Cr33Ni3Mo.



## 8. Conclusion

- I. A novel experimental set-up was developed that mimics the harsh environment in the boiler. By placing a large KCl source up-stream of the samples, the gas stream was saturated with KCl, which minimised salt evaporation from the sample surfaces. The results of the robustness tests showed that the system is reliable and can be used to carry out long-term exposures without any position-dependent corrosion.
- II. The results of the corrosion tests of the bulk materials and overlay weld coatings show that all the alloys experience breakaway oxidation and transition into secondary protection, i.e., forming outward-growing and inward-growing scales. The oxide scale thickness and microstructural investigations show that the bulk materials exhibit better corrosion resistance than the overlay weld coatings of the same composition. The improved secondary protection exhibited by the bulk materials is attributed to faster formation of more-protective chromium-rich oxides in the inward-growing scales, which is dependent upon the alloy microstructure, i.e., alloy grain size.
- III. The investigations of the microstructural evolution of selected chromia-forming and alumina-forming alloys exposed for 168, 1,000 and 8,000 hours show differences in the oxidation kinetics and oxide microstructures. In all cases, scale growth follows a diffusion-controlled process. SVM12 (12 wt% Cr) forms fast-growing oxide scales that consist of iron-rich oxides in the outer scales and spinel oxide in the inner scales, for all exposure times. The high-alloy steels, i.e., APMT and Alloy 27Cr33Ni3Mo, display slower oxidation kinetics and form thinner scales. After 168 hours of exposure, these alloys form spinel oxides in the outer and inner scales. However, as oxidation progresses, the inward-growing spinel transforms into a more-protective, chromium-rich corundum type of oxide. Alloy 27Cr33Ni3Mo displays the best secondary protection owing to an increased corundum fraction in the inner scale, which is due to phase transformation. The experimental observations agree well with the results of the thermodynamic calculations and kinetic simulations.



## 9. Future work

### *Influence of KCl + HCl on the corrosion resistance of materials*

To understand further the corrosion behaviours of materials for applications in boiler environments, it is necessary to investigate the effects of other chloride compounds and combinations that are present in the flue gas. Steel chlorination by HCl is a well-established phenomenon that affects the metallic components in boiler environments. However, there is limited knowledge regarding the combined effect of KCl and HCl on materials relevant to applications as boiler components. Therefore, the effects of HCl, alone and in combination with KCl, will be investigated in the future.

### *Corrosion studies in commercial biomass-fired and waste-fired boilers*

In the future, selected materials and coatings studied under the laboratory environment described in this thesis will be exposed to biomass-fired and waste-fired boiler environments, to understand their corrosion behaviours in the complex boiler environment. The results obtained from the field studies will be compared to the laboratory investigations to gain further insights into the corrosion behaviour.

### *Mechanism of alloy grain refinement in austenitic stainless steels*

The phenomenon of alloy grain refinement in austenitic stainless steels was observed during the corrosion investigations of this thesis. Similar observations have been made in related investigations. However, the mechanism and effect of alloy grain refinement during metal oxidation are not well-understood. It would be of interest to investigate the phenomenon of alloy grain refinement during oxidation and its effect on the high-temperature corrosion of metals.

### *Effect of Cl on secondary protection of high-temperature alloys*

The corrosive nature of alkali chlorides toward boiler materials is well-documented. However, the role of Cl in the secondary corrosion regime remains unclear. It is of interest to gain further insights into the role of Cl in the corrosion behaviours of boiler steels, beyond breakaway oxidation.



## 10. Reference

- [1] IEA, Key World Energy Statistics 2021, Paris, 2021. <https://www.iea.org/reports/key-world-energy-statistics-2021>.
- [2] B.R. (eds. ) H.-O. Pörtner, D.C. Roberts, M. Tignor, E.S. Poloczanska, K. Mintenbeck, A. Alegría, M. Craig, S. Langsdorf, S. Löschke, V. Möller, A. Okem, Climate Change 2022: Impacts, Adaptation, and Vulnerability. Contribution of Working Group II to the Sixth Assessment Report, Cambridge, 2022. <https://doi.org/doi:10.1017/9781009325844>.
- [3] K.F. Myers, P.T. Doran, J. Cook, J.E. Kotcher, T.A. Myers, Consensus revisited: quantifying scientific agreement on climate change and climate expertise among Earth scientists 10 years later, *Environmental Research Letters*. 16 (2021) 104030. <https://doi.org/10.1088/1748-9326/ac2774>.
- [4] N. Oreskes, The Scientific Consensus on Climate Change, *Science* (1979). 306 (2004) 1686. <https://doi.org/10.1126/science.1103618>.
- [5] C. Yin, S. Li, Advancing grate-firing for greater environmental impacts and efficiency for decentralized biomass/wastes combustion, *Energy Procedia*. 120 (2017) 373–379. <https://doi.org/10.1016/J.EGYPRO.2017.07.220>.
- [6] D.S. Gunarathne, P. Mellin, W. Yang, M. Pettersson, R. Ljunggren, Performance of an effectively integrated biomass multi-stage gasification system and a steel industry heat treatment furnace, *Appl Energy*. 170 (2016) 353–361. <https://doi.org/10.1016/J.APENERGY.2016.03.003>.
- [7] J. Pettersson, H. Asteman, J.-E. Svensson, L.-G. Johansson, KCl Induced Corrosion of a 304-type Austenitic Stainless Steel at 600°C; The Role of Potassium, *Oxidation of Metals*. 64 (2005) 23–41. <https://doi.org/10.1007/s11085-005-5704-3>.
- [8] J. Pettersson, C. Pettersson, H. Asteman, J.-E. Svensson, L.-G. Johansson, A pilot plant study of the effect of alkali salts on initial stages of the high temperature corrosion of alloy 304L, *Materials Science Forum*. 461–464 (2004) 965–972.
- [9] S. Kiamehr, K. v Dahl, M. Montgomery, M.A.J. Somers, KCl-induced high temperature corrosion of selected commercial alloys; KCl-induced high temperature corrosion of selected commercial alloys, (2015). <https://doi.org/10.1002/maco.201408213>.
- [10] J. Phother-Simon, I. Hanif, J. Liske, T. Jonsson, The influence of a KCl-rich environment on the corrosion attack of 304 L: 3D FIB/SEM and TEM investigations, *Corros Sci*. 183 (2021) 109315. <https://doi.org/10.1016/J.CORSCI.2021.109315>.
- [11] Y.C. Malede, J.P. Simon, T. Jonsson, M. Montgomery, K. v Dahl, J. Hald, KCl-induced corrosion of Ni-based alloys containing 35–45 wt% Cr, *Materials and Corrosion*. 70 (2019) 1486–1506. <https://doi.org/https://doi.org/10.1002/maco.201810658>.
- [12] N. Israelsson, K. Hellström, J.-E. Svensson, L.-G. Johansson, KCl-Induced Corrosion of the FeCrAl Alloy Kanthal® AF at 600 °C and the Effect of H<sub>2</sub>O, *Oxidation of Metals*. 83 (2015) 1–27. <https://doi.org/https://doi.org/10.1007/s11085-014-9506-3>.
- [13] J. Sui, J. Lehmusto, M. Bergelin, M. Hupa, The Effects of KCl, NaCl and K<sub>2</sub>CO<sub>3</sub> on the High-Temperature Oxidation Onset of Sanicro 28 Steel, *Oxidation of Metals*. 85 (2016) 565–598. <https://doi.org/https://doi.org/10.1007/s11085-016-9613-4>.

- [14] J. Pettersson, N. Folkesson, L.-G. Johansson, J.-E. Svensson, The Effects of KCl, K<sub>2</sub>SO<sub>4</sub> and K<sub>2</sub>CO<sub>3</sub> on the High Temperature Corrosion of a 304-Type Austenitic Stainless Steel, *Oxidation of Metals*. 76 (2011) 93–109. <https://doi.org/https://doi.org/10.1007/s11085-011-9240-z>.
- [15] S. Enestam, D. Bankiewicz, J. Tuiremo, K. Mäkelä, M. Hupa, Are NaCl and KCl equally corrosive on superheater materials of steam boilers?, (2012). <https://doi.org/10.1016/j.fuel.2012.07.020>.
- [16] S. Karlsson, J. Pettersson, L.-G. Johansson, J.-E. Svensson, Alkali Induced High Temperature Corrosion of Stainless Steel: The Influence of NaCl, KCl and CaCl<sub>2</sub>, *Oxidation of Metals*. 78 (2012) 83–102. <https://doi.org/https://doi.org/10.1007/s11085-012-9293-7>.
- [17] L. Reddy, M. Sattari, C.J. Davis, P.H. Shipway, M. Halvarsson, T. Hussain, Influence of KCl and HCl on a laser clad FeCrAl alloy: In-Situ SEM and controlled environment High temperature corrosion, *Corros Sci*. 158 (2019) 108076. <https://doi.org/10.1016/J.CORSCI.2019.07.003>.
- [18] J. Eklund, I. Hanif, S. Bigdeli, T. Jonsson, High temperature corrosion behavior of FeCrAlSi model alloys in the presence of water vapor and KCl at 600 °C – The influence of Cr content, *Corros Sci*. 198 (2022) 110114. <https://doi.org/10.1016/J.CORSCI.2022.110114>.
- [19] J. Lehmusto, P. Yrjas, B.J. Skrifvars, M. Hupa, High temperature corrosion of superheater steels by KCl and K<sub>2</sub>CO<sub>3</sub> under dry and wet conditions, *Fuel Processing Technology*. 104 (2012) 253–264. <https://doi.org/10.1016/J.FUPROC.2012.05.020>.
- [20] K.O. Davidsson, L.-E. Åmand, B. Leckner, B. Kovacevik, M. Svane, M. Hagström, J.B.C. Pettersson, J. Pettersson, H. Asteman, J.-E. Svensson, L.-G. Johansson, Potassium, Chlorine, and Sulfur in Ash, Particles, Deposits, and Corrosion during Wood Combustion in a Circulating Fluidized-Bed Boiler, (2007). <https://doi.org/10.1021/ef060306c>.
- [21] T. Jonsson, B. Pujilaksono, A. Fuchs, J.E. Svensson, L.G. Johansson, M. Halvarsson, The influence of H<sub>2</sub>O on iron oxidation at 600°C: A microstructural study, *Materials Science Forum*. 595–598 (2008) 1005–1012. <https://doi.org/10.4028/www.scientific.net/MSF.595-598.1005>.
- [22] D.J. Young, Corrosion in Complex Environments, *High Temperature Oxidation and Corrosion of Metals*. (2016) 603–645. <https://doi.org/10.1016/B978-0-08-100101-1.00012-1>.
- [23] S.C. Okoro, S. Kiamehr, M. Montgomery, F.J. Frandsen, K. Pantleon, Effect of flue gas composition on deposit induced hightemperature corrosion under laboratory conditionsmimicking biomass firing. Part I: Exposures in oxidizingand chlorinating atmospheres, *Materials and Corrosion*. 68 (2017) 499–514. <https://doi.org/10.1002/maco.201609173>.
- [24] H. Kassman, J. Pettersson, B.-M. Steenari, L.-E. Åmand, Two strategies to reduce gaseous KCl and chlorine in deposits during biomass combustion — injection of ammonium sulphate and co-combustion with peat, *Fuel Processing Technology*. 105 (2013) 170–180. <https://doi.org/https://doi.org/10.1016/j.fuproc.2011.06.025>.
- [25] K. Sipilä, Cogeneration, biomass, waste to energy and industrial waste heat for district heating, *Advanced District Heating and Cooling (DHC) Systems*. (2016) 45–73. <https://doi.org/10.1016/B978-1-78242-374-4.00003-3>.
- [26] Directorate-General for Energy, Review of the Reference Values for High-Efficiency Cogeneration, United Kingdom, 2015. <https://doi.org/Ref: ED59519>.

- [27] IEA, Energy Efficiency Indicators for Public Electricity Production from Fossil Fuels, Paris, 2008. <https://www.iea.org/reports/energy-efficiency-indicators-for-public-electricity-production-from-fossil-fuels> (accessed March 10, 2023).
- [28] J.R. Keiser, W.B.A. (Sandy) Sharp, D.L. Singbeil, P.M. Singh, L.A. Frederick, J.F. Meyer, IMPROVING HEAT RECOVERY IN BIOMASS-FIRED BOILERS, Oak Ridge, 2013. <https://info.ornl.gov/sites/publications/files/Pub44810.pdf>.
- [29] N. Scarlat, J.F. Dallemand, F. Monforti-Ferrario, M. Banja, V. Motola, Renewable energy policy framework and bioenergy contribution in the European Union – An overview from National Renewable Energy Action Plans and Progress Reports, Renewable and Sustainable Energy Reviews. 51 (2015) 969–985. <https://doi.org/10.1016/J.RSER.2015.06.062>.
- [30] J.R. Centre, Brief on biomass for energy in the European Union, 2019. <https://doi.org/10.2760/546943>.
- [31] A. Thorenz, L. Wietschel, D. Stindt, A. Tuma, Assessment of agroforestry residue potentials for the bioeconomy in the European Union, J Clean Prod. 176 (2018) 348–359. <https://doi.org/10.1016/J.JCLEPRO.2017.12.143>.
- [32] S. Caillat, E. Vakkilainen, Large-scale biomass combustion plants: an overview, Biomass Combustion Science, Technology and Engineering. (2013) 189–224. <https://doi.org/10.1533/9780857097439.3.189>.
- [33] C. Yin, L.A. Rosendahl, S.K. Kær, Grate-firing of biomass for heat and power production, Prog Energy Combust Sci. 34 (2008) 725–754. <https://doi.org/10.1016/J.PECS.2008.05.002>.
- [34] Babcock & Wilcox Company, Fluidized Bed boiler, (n.d.).
- [35] A. Corcoran, J. Marinkovic, F. Lind, H. Thunman, P. Knutsson, M. Seemann, Ash Properties of Ilmenite Used as Bed Material for Combustion of Biomass in a Circulating Fluidized Bed Boiler, Energy & Fuels. 28 (2014) 7672–7679. <https://doi.org/10.1021/ef501810u>.
- [36] International Standard Organization, Carbon and low alloy cast steels for general applications (ISO Standard No. 14737:2021), 3rd ed., 2021. <https://www.iso.org/standard/79985.html> (accessed March 13, 2023).
- [37] International Organization for Standardization, Stainless steels — Chemical composition (ISO Standard No. 15510:2014), 2nd ed., 2014. <https://www.iso.org/standard/61187.html> (accessed March 10, 2023).
- [38] Gosudarstvenny Standarty State Standard, HIGH-ALLOY STEELS AND CORROSION-PROOF, HEAT-RESISTING AND HIGH-TEMPERATURE ALLOYS - GOST 5632-72, M.I. Maksimova, STANDARDS PUBLISHING HOUSE, Moscow, 1975.
- [39] H. Josefsson, F. Liu, J.-E. Svensson, M. Halvarsson, L.-G. Johansson, Oxidation of FeCrAl alloys at 500–900°C in dry O<sub>2</sub>, Materials and Corrosion. 56 (2005) 801–805. <https://doi.org/https://doi.org/10.1002/maco.200503882>.
- [40] Y.S. Li, Y. Niu, M. Spiegel, High temperature interaction of Al/Si-modified Fe–Cr alloys with KCl, Corros Sci. 49 (2007) 1799–1815. <https://doi.org/https://doi.org/10.1016/j.corsci.2006.10.019>.
- [41] J. Eklund, M.D. Paz, B. Jönsson, J. Liske, J.-E. Svensson, T. Jonsson, Field exposure of FeCrAl model alloys in a waste-fired boiler at 600°C: The influence of Cr and Si on the corrosion behaviour, Materials and Corrosion. 70 (2019) 1476–1485. <https://doi.org/https://doi.org/10.1002/maco.201810618>.

- [42] J. Eklund, B. Jönsson, A. Persdotter, J. Liske, J.-E. Svensson, T. Jonsson, The influence of silicon on the corrosion properties of FeCrAl model alloys in oxidizing environments at 600 °C, *Corros Sci.* 144 (2018) 266–276. <https://doi.org/https://doi.org/10.1016/j.corsci.2018.09.004>.
- [43] J.M. Wheeldon, J.P. Shingledecker, Materials for boilers operating under supercritical steam conditions, *Ultra-Supercritical Coal Power Plants: Materials, Technologies and Optimisation*. (2013) 81–103. <https://doi.org/10.1533/9780857097514.1.81>.
- [44] M. Subanović, J. Pirón, A. Gauss, M. Jarrar, A. Schneider, SUPER VM12- A NEW 12% CR BOILER STEEL, in: J. Shingledecker, M. Takeyama (Eds.), *Joint EPRI – 123HiMAT International Conference on Advances in High-Temperature Materials*, A S M International, Nagasaki, Japan, 2019: pp. 205–216.
- [45] M.M.A. Bepari, K.M. Shorowordi, Effects of molybdenum and nickel additions on the structure and properties of carburized and hardened low carbon steels, *J Mater Process Technol.* 155–156 (2004) 1972–1979. <https://doi.org/https://doi.org/10.1016/j.jmatprotec.2004.04.060>.
- [46] J. You, H.G. Kim, J. Lee, H.-H. Kim, Y. Cho, B.-S. Jeong, K. Kang, H.M. Lee, H.N. Han, M. Kim, S.-H. Hong, Effects of molybdenum addition on microstructure and mechanical properties of Fe-B-C sintered alloys, *Mater Charact.* 173 (2021) 110915. <https://doi.org/https://doi.org/10.1016/j.matchar.2021.110915>.
- [47] inQbrands, Boiler Steel Tube Price, (2023). <https://www.made-in-china.com/> (accessed February 20, 2023).
- [48] E. Sadeghi, N. Markocsan, S. Joshi, Advances in Corrosion-Resistant Thermal Spray Coatings for Renewable Energy Power Plants. Part I: Effect of Composition and Microstructure, *Journal of Thermal Spray Technology.* 28 (2019) 1749–1788. <https://doi.org/10.1007/s11666-019-00938-1>.
- [49] Frank B. Quinlan, Lloyd P. Grobe, *TREATMENT OF METALS*, 2,303,869, 1942.
- [50] S. Zanzarin, S. Bengtsson, A. Molinari, Study of dilution in laser cladding of a carbon steel substrate with Co alloy powders, *Powder Metallurgy.* 59 (2016) 85–94. <https://doi.org/10.1080/00325899.2015.1118842>.
- [51] S.S. Sandhu, A.S. Shahi, Metallurgical, wear and fatigue performance of Inconel 625 weld claddings, *J Mater Process Technol.* 233 (2016) 1–8. <https://doi.org/10.1016/j.jmatprotec.2016.02.010>.
- [52] D.J. Young, Chapter 2 - Enabling Theory, in: D.J. Young (Ed.), *High Temperature Oxidation and Corrosion of Metals (Second Edition)*, Elsevier, 2016: pp. 31–84. <https://doi.org/https://doi.org/10.1016/B978-0-08-100101-1.00002-9>.
- [53] S. Bigdeli, L. Kjellqvist, R. Naraghi, L. Höglund, H. Larsson, T. Jonsson, Strategies for High-Temperature Corrosion Simulations of Fe-Based Alloys Using the Calphad Approach: Part I, *J Phase Equilibria Diffus.* 42 (2021) 403–418. <https://doi.org/10.1007/s11669-021-00893-x>.
- [54] N Cabrera, N F Mott, Theory of the oxidation of metals, *Reports on Progress in Physics.* 12 (1949) 163. <https://doi.org/10.1088/0034-4885/12/1/308>.
- [55] C. Wagner, Beitrag zur Theorie des Anlaufvorgangs, *21B* (1933) 25–41. <https://doi.org/doi:10.1515/zpch-1933-2105>.
- [56] P. Kofstad, *High temperature corrosion*, Elsevier Applied Science Publishers, Crown House, Linton Road, Barking, Essex IG 11 8 JU, UK, 1988. (1988).

- [57] A. Persdotter, J. Eklund, J. Liske, T. Jonsson, Beyond breakaway corrosion – Influence of chromium, nickel and aluminum on corrosion of iron-based alloys at 600 °C, *Corros Sci.* 177 (2020) 108961. <https://doi.org/10.1016/j.corsci.2020.108961>.
- [58] J. Eklund, B. Jönsson, A. Persdotter, J. Liske, J.-E. Svensson, T. Jonsson, The influence of silicon on the corrosion properties of FeCrAl model alloys in oxidizing environments at 600 °C, *Corros Sci.* 144 (2018) 266–276. <https://doi.org/https://doi.org/10.1016/j.corsci.2018.09.004>.
- [59] B. Chattopadhyay, G.C. Wood, The transient oxidation of alloys, *Oxidation of Metals.* 2 (1970) 373–399. <https://doi.org/10.1007/BF00604477>.
- [60] G.C. Wood, High-temperature oxidation of alloys, *Oxidation of Metals.* 2 (1970) 11–57. <https://doi.org/10.1007/BF00603581>.
- [61] D. Caplan, M. Cohen, The Volatilization of Chromium Oxide, *J Electrochem Soc.* 108 (1961) 438. <https://doi.org/10.1149/1.2428106>.
- [62] F.H. Stott, G.C. Wood, J. Stringer, The influence of alloying elements on the development and maintenance of protective scales, *Oxidation of Metals.* 44 (1995) 113–145. <https://doi.org/10.1007/BF01046725>.
- [63] H.El. Kadiri, R. Molins, Y. Bienvenu, M.F. Horstemeyer, Abnormal High Growth Rates of Metastable Aluminas on FeCrAl Alloys, *Oxidation of Metals.* 64 (2005) 63–97. <https://doi.org/10.1007/s11085-005-5715-0>.
- [64] H. Asteman, J.-E. Svensson, L.-G. Johansson, M. Norell, Indication of Chromium Oxide Hydroxide Evaporation During Oxidation of 304L at 873 K in the Presence of 10% Water Vapor, *Oxidation of Metals.* 52 (1999) 95–111. <https://doi.org/https://doi.org/10.1023/A:1018875024306>.
- [65] B. Pujilaksono, T. Jonsson, M. Halvarsson, J.-E. Svensson, L.-G. Johansson, Oxidation of iron at 400–600 °C in dry and wet O<sub>2</sub>, *Corros Sci.* 52 (2010) 1560–1569. <https://doi.org/10.1016/J.CORSCI.2010.01.002>.
- [66] B. Pujilaksono, T. Jonsson, H. Heidari, M. Halvarsson, J.-E. Svensson, L.-G. Johansson, Oxidation of Binary FeCr Alloys (Fe–2.25Cr, Fe–10Cr, Fe–18Cr and Fe–25Cr) in O<sub>2</sub> and in O<sub>2</sub> + H<sub>2</sub>O Environment at 600 °C, *Oxidation of Metals.* 75 (2011) 183–207. <https://doi.org/https://doi.org/10.1007/s11085-010-9229-z>.
- [67] J. Töpfer, S. Aggarwal, R. Dieckmann, Point defects and cation tracer diffusion in (Cr<sub>x</sub>Fe<sub>1-x</sub>)<sub>3</sub> – δO<sub>4</sub> spinels, *Solid State Ion.* 81 (1995) 251–266. [https://doi.org/10.1016/0167-2738\(95\)00190-H](https://doi.org/10.1016/0167-2738(95)00190-H).
- [68] R. Dieckmann, M.R. Hilton, T.O. Mason, Defects and Cation Diffusion in Magnetite (VIII): Migration Enthalpies for Iron and Impurity Cations, *Berichte Der Bunsengesellschaft Für Physikalische Chemie.* 91 (1987) 59–66. <https://doi.org/https://doi.org/10.1002/bbpc.19870910113>.
- [69] J. Eklund, B. Jönsson, A. Persdotter, J. Liske, J.-E. Svensson, T. Jonsson, The influence of silicon on the corrosion properties of FeCrAl model alloys in oxidizing environments at 600 °C, *Corros Sci.* 144 (2018) 266–276. <https://doi.org/https://doi.org/10.1016/j.corsci.2018.09.004>.
- [70] H.W. Grünling, R. Bauer, The role of silicon in corrosion-resistant high temperature coatings, *Thin Solid Films.* 95 (1982) 3–20. [https://doi.org/10.1016/0040-6090\(82\)90578-8](https://doi.org/10.1016/0040-6090(82)90578-8).
- [71] M. McNallan, W.W. Liang, S.H. Kim, C.T. Kang, ACCELERATION OF THE HIGH TEMPERATURE OXIDATION OF METALS BY CHLORINE., *NACE.* (1983) 316–321.

- [72] H.J. Grabke, E. Reese, M. Spiegel, The effects of chlorides, hydrogen chloride, and sulfur dioxide in the oxidation of steels below deposits, *Corros Sci.* 37 (1995) 1023–1043. [https://doi.org/https://doi.org/10.1016/0010-938X\(95\)00011-8](https://doi.org/https://doi.org/10.1016/0010-938X(95)00011-8).
- [73] N. Folkesson, L.-G. Johansson, J.-E. Svensson, Initial Stages of the HCl-Induced High-Temperature Corrosion of Alloy 310, *J Electrochem Soc.* 154 (2007) C515. <https://doi.org/10.1149/1.2754174>.
- [74] V. Ssentenza, J. Eklund, I. Hanif, J. Liske, T. Jonsson, High temperature corrosion resistance of FeCr(Ni, Al) alloys as bulk/overlay weld coatings in the presence of KCl at 600 °C, *Corros Sci.* 213 (2023) 110896. <https://doi.org/10.1016/J.CORSCI.2022.110896>.
- [75] N. Israelsson, K.A. Unocic, K. Hellström, T. Jonsson, M. Norell, J.-E. Svensson, L.-G. Johansson, A Microstructural and Kinetic Investigation of the KCl-Induced Corrosion of an FeCrAl Alloy at 600 °C, *Oxidation of Metals.* 84 (2015) 105–127. <https://doi.org/10.1007/s11085-015-9546-3>.
- [76] H. Asteman, J.-E. Svensson, M. Norell, L.-G. Johansson, Influence of Water Vapor and Flow Rate on the High-Temperature Oxidation of 304L; Effect of Chromium Oxide Hydroxide Evaporation, *Oxidation of Metals.* 54 (2000) 11–26. <https://doi.org/10.1023/A:1004642310974>.
- [77] M. Halvarsson, J.E. Tang, H. Asteman, J.-E. Svensson, L.-G. Johansson, Microstructural investigation of the breakdown of the protective oxide scale on a 304 steel in the presence of oxygen and water vapour at 600 °C, *Corros Sci.* 48 (2006) 2014–2035. <https://doi.org/https://doi.org/10.1016/j.corsci.2005.08.012>.
- [78] E. Essuman, G.H. Meier, J. Zurek, M. Hänsel, L. Singheiser, W.J. Quadackers, Enhanced internal oxidation as trigger for breakaway oxidation of Fe–Cr alloys in gases containing water vapor, *Scr Mater.* 57 (2007) 845–848. <https://doi.org/10.1016/J.SCRIPTAMAT.2007.06.058>.
- [79] J. Lehmusto, M. Sattari, M. Halvarsson, L. Hupa, Should the oxygen source be considered in the initiation of KCl-induced high-temperature corrosion?, *Corros Sci.* 183 (2021) 109332. <https://doi.org/https://doi.org/10.1016/j.corsci.2021.109332>.
- [80] J.I. Goldstein, D.E. Newbury, J.R. Michael, N.W.M. Ritchie, J.H.J. Scott, D.C. Joy, *Scanning electron microscopy and X-ray microanalysis*, Third edit, Springer, 2017.
- [81] D.B. Williams, C.B. Carter, *Transmission Electron Microscopy*. [electronic resource] : A Textbook for Materials Science., 2nd ed. 20, Springer US, 2009. <https://search.ebscohost.com/login.aspx?direct=true&db=cat07472a&AN=clec.SPRINGERLIN K9780387765013&site=eds-live&scope=site&authtype=guest&custid=s3911979&groupid=main&profile=eds>.
- [82] ASTM international, *Standard Test Methods for Determining Average Grain Size*, PA 19428-2959, 2013. <https://doi.org/Designation: E112 - 12>.
- [83] H.P. Michelsen, F. Frandsen, K. Dam-Johansen, O.H. Larsen, Deposition and high temperature corrosion in a 10 MW straw fired boiler, *Fuel Processing Technology.* 54 (1998) 95–108. [https://doi.org/10.1016/S0378-3820\(97\)00062-3](https://doi.org/10.1016/S0378-3820(97)00062-3).
- [84] C. Fan, D. Pei, H. Wei, A novel cascade energy utilization to improve efficiency of double reheat cycle, *Energy Convers Manag.* 171 (2018) 1388–1396. <https://doi.org/https://doi.org/10.1016/j.enconman.2018.06.095>.

- [85] J. Kotowicz, H. Łukowicz, Ł. Bartela, S. Michalski, Validation of a program for supercritical power plant calculations, *Archives of Thermodynamics*. (2011) 81–89. <https://doi.org/10.2478/v10173-011-0033-1>.
- [86] A. Col, V. Parry, C. Pascal, Oxidation of a Fe–18Cr–8Ni austenitic stainless steel at 850 °C in O<sub>2</sub>: Microstructure evolution during breakaway oxidation, *Corros Sci*. 114 (2017) 17–27. <https://doi.org/10.1016/j.corsci.2016.10.029>.
- [87] X. Montero, A. Ishida, M. Rudolphi, H. Murakami, M.C. Galetz, Breakaway corrosion of austenitic steel induced by fireside corrosion, *Corros Sci*. 173 (2020) 108765. <https://doi.org/10.1016/j.corsci.2020.108765>.
- [88] F. Liu, J.E. Tang, T. Jonsson, S. Canovic, K. Segerdahl, J.E. Svensson, M. Halvarsson, Microstructural investigation of protective and non-protective oxides on 11% chromium steel, *Oxidation of Metals*. 66 (2006) 295–319. <https://doi.org/10.1007/s11085-006-9035-9>.
- [89] J. Pettersson, J.-E. Svensson, L.-G. Johansson, KCl-Induced Corrosion of a 304-type Austenitic Stainless Steel in O<sub>2</sub> and in O<sub>2</sub> + H<sub>2</sub>O Environment: The Influence of Temperature, *Oxidation of Metals*. 72 (2009) 159–177. <https://doi.org/10.1007/s11085-009-9153-2>.
- [90] J. Eklund, High Temperature Corrosion of FeCrAl Alloys in Biomass- and Wastefired Boilers. The Influence of Alloying Elements in Prediction and Mitigation of Corrosion in Harsh Environments, THESIS FOR THE DEGREE OF DOCTOR OF PHILOSOPHY, Chalmers University of Technology, 2020. [https://research.chalmers.se/publication/521876/file/521876\\_Fulltext.pdf](https://research.chalmers.se/publication/521876/file/521876_Fulltext.pdf).
- [91] J. Eklund, A. Persdotter, I. Hanif, S. Bigdeli, T. Jonsson, Secondary corrosion protection of FeCr(Al) model alloys at 600 °C – The influence of Cr and Al after breakaway corrosion, *Corros Sci*. 189 (2021). <https://doi.org/10.1016/J.CORSCI.2021.109584>.
- [92] N. Mortazavi, C. Geers, M. Esmaily, V. Babic, M. Sattari, K. Lindgren, P. Malmberg, B. Jönsson, M. Halvarsson, J.E. Svensson, I. Panas, L.G. Johansson, Interplay of water and reactive elements in oxidation of alumina-forming alloys, *Nat Mater*. 17 (2018) 610–617. <https://doi.org/https://doi.org/10.1038/s41563-018-0105-6>.
- [93] B.A. Pint, K.L. More, I.G. Wright, The use of two reactive elements to optimize oxidation performance of alumina-forming alloys, *Materials at High Temperatures*. 20 (2003) 375–386. <https://doi.org/10.1179/mht.2003.044>.
- [94] J. Stringer, The reactive element effect in high-temperature corrosion, *Materials Science and Engineering: A*. 120–121 (1989) 129–137. [https://doi.org/https://doi.org/10.1016/0921-5093\(89\)90730-2](https://doi.org/https://doi.org/10.1016/0921-5093(89)90730-2).
- [95] S. Mrowec, J. Jedliński, A. Gil, The influence of certain reactive elements on the oxidation behaviour of chromia- and alumina-forming alloys, *Materials Science and Engineering: A*. 120–121 (1989) 169–173. [https://doi.org/https://doi.org/10.1016/0921-5093\(89\)90735-1](https://doi.org/https://doi.org/10.1016/0921-5093(89)90735-1).
- [96] J. Eklund, A. Persdotter, I. Hanif, S. Bigdeli, T. Jonsson, Secondary corrosion protection of FeCr(Al) model alloys at 600 °C – The influence of Cr and Al after breakaway corrosion, *Corros Sci*. 189 (2021) 109584. <https://doi.org/10.1016/J.CORSCI.2021.109584>.
- [97] J.J. Barnes, G.Y. Lai, Factors affecting the nitridation behavior of Fe-base, Ni-base, and Co-base alloys in pure nitrogen, *Le Journal de Physique IV*. 03 (1993) C9-167-C9-174. <https://doi.org/10.1051/jp4:1993915>.

- [98] J. Eklund, B. Paz, Maria Dolores Jönsson, J. Liske, J.-E. Svensson, T. Jonsson, Field exposure of FeCrAl model alloys in a waste-fired boiler at 600°C: The influence of Cr and Si on the corrosion behaviour, *Materials and Corrosion*. 70 (2019) 1476– 1485.
- [99] N. Israelsson, K.A. Unocic, K. Hellström, J.-E. Svensson, L.-G. Johansson, Cyclic Corrosion and Chlorination of an FeCrAl Alloy in the Presence of KCl, *Oxidation of Metals*. 84 (2015) 269–290. <https://doi.org/10.1007/s11085-015-9554-3>.
- [100] X. Peng, J. Yan, Y. Zhou, F. Wang, Effect of grain refinement on the resistance of 304 stainless steel to breakaway oxidation in wet air, *Acta Mater*. 53 (2005) 5079–5088. <https://doi.org/10.1016/J.ACTAMAT.2005.07.019>.
- [101] V. Trindade, H.-J. Christ, U. Krupp, Grain-Size Effects on the High-Temperature Oxidation Behaviour of Chromium Steels, *Oxidation of Metals*. 73 (2010) 551–563. <https://doi.org/10.1007/s11085-010-9192-8>.
- [102] J. Eklund, A. Persdotter, V. Ssentenza, T. Jonsson, The long-term corrosion behavior of FeCrAl(Si) alloys after breakaway oxidation at 600 °C, *Corros Sci*. 217 (2023) 111155. <https://doi.org/https://doi.org/10.1016/j.corsci.2023.111155>.